Lateral solid mixing in gas-fluidized beds: CFD and DEM studies

Oyebanjo Oke[1], Berend Van Wachem[2], Luca Mazzei[1]*

[1]*Department of Chemical Engineering, University College London, WC1E 7JE, London, UK*

[2]*Division of Thermofluids, Department of Mechanical Engineering, Imperial College London, SW7 2AZ, London, UK*

*Corresponding author. Email: *l.mazzei@ucl.ac.uk*

Abstract

We investigated lateral solid mixing in gas-fluidized beds using CFD and DEM. We ran 3D CFD simulations, comparing the results with those formerly obtained in 2D CFD simulations. We observed that the frictional stress model affects the numerical results. This was also observed in 2D simulations, but in 3D simulations the effect is less pronounced. The 3D simulations described the lateral solid mixing process more accurately than the 2D simulations, simulation dimensionality being an important factor. To analyse further the role of frictional stress models, we ran 3D DEM simulations, employing the soft-sphere approach to model the particle-particle contact forces. The simulation results agreed reasonably well with the empirical data, but their accuracy depended on the values used for the collision parameters; also, the 3D CFD simulations matched the empirical data more closely. Altogether, we concluded that the simulation dimensionality plays the dominant role in predicting lateral solid mixing accurately.

Keywords: Fluidization, Multiphase flow, Mixing, Lateral dispersion, CFD, DEM.

1.0 Introduction

Gas-fluidized beds are widely used in industrial processes involving physical or chemical operations. To be efficient and safe, several of these processes require that particles be well mixed. Good mixing promotes intimate contact among particles and between the particles and the fluid, enhancing heat and mass transfer. Therefore, to design and operate fluidized beds efficiently, one should understand well the dynamics of solid mixing.

To investigate solid mixing in these systems, researchers often focus on axial and lateral mixing. The latter, in particular, is useful in assessing the performance of large-scale fluidized bed reactors (Grace, 1981). Researchers have used different experimental and theoretical methods to study the process of lateral solid mixing. They often quantify its rate using a lateral dispersion coefficient (D_{sr}). There are several studies aimed at investigating the influence of geometry (Liu & Chen, 2010; Xiao et al., 1998), operating conditions (Bellgardt et al., 1985; Chirone et al., 2004; Lim & Agarwal, 1994; Pallarès et al., 2007) and particle properties (Pallarès & Johnsson, 2006; Salam et al., 1987; Xiang et al., 1987) on lateral solid mixing in fluidized beds. Despite these investigations, the understanding of how these parameters affect the dispersion coefficient is still quite limited, because the mechanisms governing the solid mixing process are complex.

A rapid increase in computational power has made it possible to investigate multiphase flows in fluid beds numerically. Two modelling approaches are used: Eulerian-Eulerian and Eulerian-Lagrangian. In the former, averaged equations of motion describe the fluid and the solid as interpenetrating continua (Lettieri & Mazzei, 2009), while in the latter the motion of each particle is tracked and one solves the average equation of motion solely for the fluid phase (van der Hoef et al., 2008). In this work, we employed both modelling approaches to investigate lateral solid mixing. For the Eulerian-Lagrangian simulations, we used the Discrete Element Modelling (DEM) approach.

Studies on numerical simulations of lateral solid mixing in gas-fluidized beds are still limited. To the best of our knowledge, numerical works on lateral solid dispersion in these systems have only been

conducted by Liu & Chen (2010) and Farzaneh et al. (2011). The former used Eulerian-Eulerian simulations to investigate the influence of bed width and superficial gas velocity on lateral mixing, while the latter employed Eulerian-Lagrangian simulations to examine the influence of bed height and superficial gas velocity. In our previous work, we investigated the influence of design parameters and operational conditions adopting a 2D Eulerian-Eulerian modelling approach (Oke et al., 2014). We quantified the rate at which solids mix laterally via a lateral dispersion coefficient (D_{sr}). For all the cases considered, the numerical results overestimated the empirical data. We identified two possible causes. The first relates to the 2D nature of our simulations, while the second relates to how the solid-phase frictional stress is modelled constitutively. We investigated this aspect using different frictional stress models and changing the solid volume fraction value ϕ_{min} at which the bed is assumed to enter the frictional flow regime. Some frictional models resulted to be more accurate, but the overprediction was not eliminated. This work attempts to address these problems.

To begin, we addressed the issue of dimensionality. We ran 3D simulations considering the same powder, the same computational setup and the same simulation cases employed in our former 2D simulations. This allowed us to see how simulation dimensionality affects the numerical results. We also investigated the frictional stress modelling issue using DEM simulations. These offer a simpler way of describing the rheology of the solid phase. This is because we no longer need to model the solid stress, since the solid phase is not described as a continuum. Finally, we compared the results of the Eulerian-Eulerian and Eulerian-Lagrangian simulations.

2.0 Lateral dispersion coefficient – Definition and estimation

Sometimes one may want to estimate how quickly solids spread axially and laterally in the bed. To do this, researchers often resort to axial and lateral dispersion coefficients; these are *effective* diffusivities relating to the times which solids take to spread axially and laterally over a given distance in the bed. Recently, researchers have made considerable effort to investigate lateral dispersion coefficients more closely; this is because earlier studies (Avidan and Yerushalmi, 1985; Lewis et al., 1962; May,1956) concentrated mainly on axial dispersion coefficients. Notwithstanding, lateral dispersion is essential in

the design and operation of large-scale beds, the coefficient quantifying it being a key input parameter in many models for fluid bed reactors.

Most researchers define D_{sr} by means of an equation analogous to Fick's law of molecular diffusion (Borodulya et al., 1982; Liu & Chen, 2010; Oke et al., 2015; Shi & Fan, 1984), thus writing:

$$\partial_t C = D_{sr} \partial_{xx}^2 C \tag{1}$$

where C is the void-free solid density, D_{sr} is the lateral dispersion coefficient, t is the time and x is the spatial coordinate associated with the horizontal direction along which lateral mixing takes place. This equation, as said, *defines* the dispersion coefficient.

Consider a bed in which the concentration of solid depends on the time and on the spatial coordinates, so that $c = c(x, y, z, t)$. The concentration in Eq. 1 is averaged over the vertical direction (associated with the spatial coordinate y) and one horizontal direction (associated with the spatial coordinate z); in other words, it is averaged over the vertical plane yz. The mean concentration C is thus a function merely of t and of the spatial coordinate x. For a given system, by matching the actual concentration function $C_e(x, t)$, which one can determine either experimentally or numerically, with the analytical solution of Eq. 1, one can obtain the value of the lateral dispersion coefficient. We should bear in mind that, unlike molecular diffusion coefficients, D_{sr} is *not* just a function of the particle properties, but depends on the system geometry and on the operating conditions.

In this work, we considered a bed divided into two equal compartments: one extending from $x = 0$ to $x = L/2$ and one extending from $x = L/2$ to $x = L$, where L is the width of the bed in the x direction. The particles occupying them differed only in colour (in particular, having same size and density). We placed red particles in the left compartment and blue particles in the other. $c(x, y, z, t)$ and $C(x, t)$ are the concentrations of one kind of particles, say the red ones, which are regarded as tracer particles. So, the initial conditions characterizing this setup are:

$$t = 0: \quad C = \bar{C} \quad for \quad 0 \leq x < L/2 \quad and \; C = 0 \; for \; L/2 < x \leq L \tag{2}$$

The boundary conditions assigned are:

$$x = 0, \quad x = L: \qquad \partial_x C = 0 \tag{3}$$

The compartments were separated by a removable wall. At $t = 0$, we fluidized the system, waiting for it to reach pseudo-stationary conditions (the system reached this state within three real-time seconds). Subsequently, we removed the wall, letting red and blue particles spread through the bed, and we calculated the void-free concentration $c(x, y, z, t)$ of red particles. We then divided the bed in a number of vertical layers (obtained by slicing the bed with imaginary planes parallel to the yz plane) and calculated the mean value of C_e in each layer using the relation:

$$C_e(x, t) \equiv \frac{1}{V_L} \int_{V_L} c(x, y, z, t) dV \tag{4}$$

where V_L is the volume of each layer (all layers were identical). The next step was solving Eq. 1 with the conditions given in Eqs. 2 and 3. For this system the analytical solution, reported by Hirama et al. (1975), is:

$$\frac{C(x, t; D_{sr})}{\bar{C}} = \frac{1}{2} + \frac{2}{\pi} \sum_{a=1}^{\infty} \frac{1}{a} sin\left(\frac{a\pi}{2}\right) cos\left(a\pi \frac{x}{L}\right) exp\left(-a^2\pi^2 \frac{t}{L^2/D_{sr}}\right) \tag{5}$$

Here we have reported explicitly the dependence of the analytical solution C on the parameter D_{sr}. To estimate D_{sr} we then matched the profiles $C_e(x, t)$ and $C(x, t; D_{sr})$. To do this, we defined:

$$G \equiv [C(x, t; D_{sr}) - C_e(x, t)]^2 \tag{6}$$

The task of determining D_{sr} reduced to finding the value of D_{sr} that minimizes G in Eq. 6. This gave the value of the lateral dispersion coefficient for the system under investigation.

We would like to emphasize that the parameter D_{sr} in Eq. 1 is different from the coefficient appearing in the original Fick's law. In the latter the parameter is molecular diffusivity, which is constant for a solute in a given solvent. Fick's law relates to the diffusion of molecules generated by their random motion. The lateral dispersion coefficient, conversely, is affected by various competing mechanisms. These, as experimental evidence reveals, include bubble break-up at the upper surface of the bed and subsequent ejection of particles into the freeboard, wake transport and drifting of emulsion owing to

the passage of bubbles. The lateral dispersion coefficient is thus affected by many variables, among which we find bubble size and velocity, particle size and density as well as fluid density and viscosity. Shi & Fan (1984) reported that lateral mixing is also affected by gross particle circulation, this in turn depending on bed height and superficial gas velocity. Determining D_{sr} is thus quite challenging.

3.0 Eulerian-Eulerian model

The governing equations in this modelling approach consist of averaged balance equations for mass and linear momentum written for the fluid and for two solid phases (red and blue particles). We do not report these equations, since their formulation is standard and can be found in the literature (Oke et al., 2014; Tagliaferri et al., 2013). The equations are unclosed; the fluid-particle interaction force, the effective stress tensor of the fluid and particle phases and the particle-particle interaction force need to be expressed constitutively. These constitutive equations can be found in Oke et al. (2014).

4.0 DEM model

The DEM model tracks each particle using Newton's second law of dynamics; the motion of the fluid phase is described using the averaged equations of motion (the same adopted in the Eulerian-Eulerian model). In modelling particle-particle interactions, one can regard the particles either as *hard spheres* or as *soft spheres*. In this work, we used the soft-sphere model because it can handle dense granular flows, where particles interact through multiple and sustained contacts.

The soft-sphere model was proposed by Cundall & Strack (1979). In this framework, particles are allowed to overlap slightly at the collision points, where the amount of overlap is directly proportional to the amount of deformation at the contact point. The forces are then determined by relating them to the deformation at the contact point with an appropriate constitutive model (van Wachem & Almstedt, 2003). The soft-sphere model allows for multiple as well as enduring contacts; the net contact force at any time is given by the sum of all the pair-wise interactions occurring at that time. The governing equations of the model are reported in the next sections.

4.1 Equations of motion

The motion of every particle is described by Newton's second law:

$$m_i \frac{d\boldsymbol{v}_i}{dt} = \beta_i \frac{V_i}{\phi}(\boldsymbol{u}_e - \boldsymbol{v}_i) + m_i \boldsymbol{g} - V_i \nabla p + \sum_j (\boldsymbol{F}_{ij,n} + \boldsymbol{F}_{ij,t}) \quad (7)$$

where m_i is the particle mass, $\boldsymbol{v}_i$ is the particle velocity, $\boldsymbol{u}_e$ is the local undisturbed fluid velocity, $\boldsymbol{g}$ is the gravitational acceleration, V_i is the particle volume, ∇p is the fluid pressure gradient, ϕ is the particle volume fraction, $\boldsymbol{F}_{ij,n}$ and $\boldsymbol{F}_{ij,t}$ are the normal and tangential components of the contact force $\boldsymbol{F}_{ij}$ exerted by particle j on particle i and β_i is the interphase momentum transfer coefficient. Other force contributions, such as the virtual mass and lift forces, are neglected. We used the expression of Mazzei & Lettieri (2007) to close the interphase momentum transfer coefficient.

The evolution of the angular momentum of each particle is described by:

$$I_i \frac{d\boldsymbol{\omega}_i}{dt} = \sum_{\boldsymbol{j}} (R_i \boldsymbol{n}_{ij} \times \boldsymbol{F}_{ij,t}) \quad (8)$$

where I_i is the moment of inertia of the particle, $\boldsymbol{\omega}_i$ is the rotational velocity, $\boldsymbol{n}_{ij}$ is the unit vector joining the centre of particle i to that of particle j and R_i is the radius of particle i. By integrating the equations of motion, using the Verlet algorithm (Mallouppas & van Wachem, 2013), we obtained the evolution in time of the particle positions and velocities.

4.2 Contact force

In this work, particle collisions were modelled using the soft-sphere approach proposed by Cundall & Strack (1979), using the contact models of Tsuji et al. (1992) for the normal forces and Mindlin & Deresiewicz (1953) for the tangential forces.

When particle i is in contact with particle j, the normal contact force $\boldsymbol{F}_{ij,n}$ acting on particle i is given by the contribution of a Hertzian elastic repulsion and a visco-elastic damping:

$$\boldsymbol{F}_{ij,n} = -[K_n {\delta_n}^{3/2} + \eta_n (\boldsymbol{v}_{ij}.\boldsymbol{n}_{ij})]\boldsymbol{n}_{ij} \quad (9)$$

where K_n is the material stiffness constant and η_n determines the amount of damping (Mindlin & Deresiewicz, 1953). Moreover, letting $\boldsymbol{r}_i$ and $\boldsymbol{r}_j$ denote the position vectors of the centres of particles *i* and *j*, respectively, it is:

$$\boldsymbol{v}_{ij} = \left(\boldsymbol{v}_i - \boldsymbol{v}_j\right) + \left(R_i\boldsymbol{\omega_i} + R_j\boldsymbol{\omega_j}\right) \times \boldsymbol{n}_{ij} \quad ; \quad \delta_n = \left(R_i + R_j\right) - \left|\boldsymbol{r}_i - \boldsymbol{r}_j\right| \tag{10}$$

The expression for the tangential component of the contact force depends on whether particles i and j slide on each other (kinetic friction) or not (static friction). If there is no-slip in the contact point, the Mindlin & Deresiewicz (1953) model is used, including a tangential dampening:

$$\boldsymbol{F}_{ij,t} = -\left[K_t\delta_t + \eta_t(\boldsymbol{v}_{ij}.\boldsymbol{t}_{ij})\right]\boldsymbol{t}_{ij} \tag{11}$$

where K_t, δ_t, η_t and $\boldsymbol{t}_{ij}$ are the material stiffness, the displacement, the damping coefficient and the unit vector, all in the tangential direction. It is emphasised that the model for the tangential forces is determined in an incremental fashion, where the change in the tangential force is determined by the change in tangential overlap and tangential overlap direction during each time step. For further detail, see van Wachem et al. (2015). If at a time step the cumulative tangential force exceeds the coulomb slip force, *i.g.*, $|\boldsymbol{F}_{ij,t}| > \mu\left|\boldsymbol{F}_{ij,n}\right|$, where μ is the friction coefficient, particles i and j begin to slide and the tangential force is clipped to this value and replaced by:

$$\boldsymbol{F}_{ij,t} = -\mu\left|\boldsymbol{F}_{ij,n}\right|\boldsymbol{t}_{ij} \tag{12}$$

4.3 Material stiffness

For two spheres of equal size, the normal material stiffness constant is given by the following expression obtained from the Hertian contact theory (Johnson, 1987):

$$K_n = \frac{\sqrt{2R_i}E_i}{3(1-{\sigma_i}^2)} \tag{13}$$

where E_i is the Young modulus and σ_i is the Possion ratio of particle i. In the case of contact between a sphere and a wall, letting E_w and σ_w denote the Young modulus and Poisson ratio of the wall, K_n is given by the following relation:

$$K_n = \frac{\frac{4\sqrt{R_i}}{3}}{\frac{1-{\sigma_i}^2}{E_i} + \frac{1-{\sigma_w}^2}{E_w}} \tag{14}$$

The relation for calculating the tangential material stiffness constant was derived by Mindlin (1949) and Mindlin & Deresiewicz (1953) and reads:

$$K_t = \frac{2\sqrt{2R_i}G_i}{2-\sigma_i}{\delta_n}^{1/2} \tag{15}$$

where G_i is the shear modulus of particle i. This is related to the Young modulus E_i and to the Poisson ratio σ_i as follows:

$$G_i = \frac{E_i}{2(1+\sigma_i)} \tag{16}$$

For the case of contact between a particle and the wall, Tsuji et al. (1992) provides the following expression for calculating the tangential material stiffness constant:

$$K_t = \frac{8\sqrt{R_i}G_i}{2-\sigma_i}{\delta_n}^{1/2} \tag{17}$$

4.4 Damping coefficient

Following van Wachem et al. (2010), we used the following expressions for the damping coefficients, describing the inelastic nature of the material due to its visco-elastic properties:

$$\eta_n = \alpha\sqrt{MK_n}\,{\delta_n}^{1/4} \quad ; \quad \eta_t = \alpha\sqrt{MK_t}\,{\delta_t}^{1/4} \tag{18}$$

For collisions between particles i and j, it is:

$$M = \frac{m_i m_j}{(m_i + m_j)} \tag{19}$$

For collisions between particle i and the wall, $M = \alpha m_i$, where α is a parameter that depends on the coefficient of restitution e. This dependence is well defined by Tsuji et al. (1992).

The application of realistic values for the Young's modulus will lead to very high values of K_n and K_t. Therefore, very often unrealistic values for the Young's modulus are employed, otherwise the integration time step required in the simulation becomes impractically small (Gera et al., 1998;

Kaneko et al., 1999; Kawaguchi et al., 1998; Mikami et al., 1998; Rhodes et al., 2001; Rong et al., 1999; Tian et al., 2007). Albeit this value reduces the computational effort considerably, there is a risk that the accuracy of the simulation results might be affected (Di Renzo & Di Maio, 2004). All these aspects have been examined in this work and will be discussed in the Section 7.

5.0 Boundary and initial conditions

In the 3D CFD simulations, no-slip boundary conditions were applied on all the walls of the system and on the partition plate (when present) for all phases. These wall boundary conditions were used as well in the DEM simulations for the fluid phase (for the particles no boundary conditions are needed on walls). In the 2D CFD simulations front and back wall effects were neglected (because these walls were not accounted for, owing to the simulation dimensionality). At the bottom of the bed, a uniform inlet fluid velocity was specified. At the domain upper boundary, the pressure was set to 10E5 Pa.

In all the CFD simulations, in its initial state the bed was fixed and made up of a uniform powder with volume fraction equal to 0.60 (so, the voidage was set everywhere to 0.40) and the fluid was stagnant. In all the DEM simulations, the same initial conditions were used, with the particles packed randomly.

6.0 Numerical schemes and techniques

To run the Eulerian-Eulerian simulations, we employed the commercial CFD code Fluent 12.1 (by Ansys). The governing and constitutive equations were implemented in the multi-fluid model of the package, which is based on an Eulerian description of the flow. We used the pressure-based solver, which is recommended for low-speed incompressible flows. To convert scalar transport equations into algebraic equations that can be solved numerically, the code employs a finite-volume discretization scheme. We discretized in space through a second-order upwind scheme and in time through a first-order implicit scheme. To couple pressure and velocity, we used the SIMPLE (Simultaneous Solution of Non-linearly Coupled Equations) algorithm of Lo (1989); the code does not allow other coupling algorithms for Eulerian multiphase calculations. At each time step, we employed a maximum of 250 iterations to compute the flow variables. Setting the tolerance to 10E-5, we attained convergence

within the iteration limit. The time step was set to 10E-3 s, and under-relaxation factors of 0.20 were used for all the variables. The computational grid was uniform with square (in 2D) and cubic (in 3D) cells of 5 mm side (this is the same mesh used in the 2D simulations reported in Oke et al., 2014). To post-process and visualize the results of the simulations we used the data analysis software included in the Ansys 12.1 package.

The setup just described (as well as the balance and constitutive equations) is the same as that used by Oke et al. (2014). This ensures that the simulations of this work are consistent with those previously conducted, so that comparing their results is meaningful.

To run the Eulerian-Lagrangian simulations, we used the in-house DEM code MultiFlow developed by Professor Berend van Wachem at Imperial College London (http://www.multiflow.org/). The code tracks the properties of individual particles and of the fluid at the particle location. It achieves this by determining (by interpolation) the Eulerian properties of the fluid at the center of the particle and by creating a particle mesh which is used to generate collision-neighbour finding lists. The particle mesh (whose sole purpose, as said, is to find the nearest neighbours of each particle) is a fictitious uniform Cartesian mesh with call size equal to 1.5 times the particle diameter. Similar to the Eulerian-Eulerian simulations, the discretization of the Eulerian fluid-phase equation of motion is conducted via a finite volume approach, combined with a second-order accurate central difference scheme for the advection terms and a second-order accurate, three-point backward Euler discretization scheme for the temporal term. The pressure-velocity coupling is done in a fully-coupled framework, using one outer iteration per time-step (van Wachem et al., 2007). The governing and constitutive equations for the particles reported in Section 4 were already included in the package. To post-process and visualize the results of the simulations we used ParaView, an open-source, multi-platform visualization and data analysis application (http://www.paraview.org/).

7.0 Results and discussions

As discussed above, one of the aims of the present work is to investigate the influence of simulation dimensionality on the numerical prediction of D_{sr}. We believe that the overestimation of the latter in our previous work (Oke et al., 2014) is partly due to the 2D nature of our simulations; hence, we ran simulations in 3D using the Eulerian-Eulerian model, adopting the same computational setup used in our 2D simulations. The geometry employed is also the same as the one used in the latter simulations, except that this is three-dimensional.

7.1 Eulerian-Eulerian simulations - 2D versus 3D

From the solid volume fraction spatial profiles obtained numerically, we calculated the void-free mass fraction $\hat{\phi}_i\,(x,t)$ and concentration $C_i(x,t)$ of solid phase i in each layer:

$$\hat{\phi}_i(x,t) \equiv \frac{C_i\,(x,t)}{\bar{C}} \equiv \frac{\phi_i\,(x,t)}{\phi_1(x,t)+\phi_2(x,t)} \tag{20}$$

We ran simulations at various superficial gas velocities, keeping the minimum fluidization bed height at 5.23 cm, bed width at 0.6 m, and bed depth at 5 cm. These dimensions are those of the system investigated experimentally by Shi & Fan (1984), whose data we used to validate our numerical results. We fitted the void-free mass fraction profiles obtained from our simulations with those obtained from Eq. 5 using the least square regression method, as reported above. The values of D_{sr} obtained at a superficial gas velocity of 0.87 m/s at different computational times for 2D and 3D simulations are reported in Figure 1. In the latter we observe that D_{sr} values initially increase and then attain a stable value. The initial increase in D_{sr} values can be attributed to the sudden removal of the partition wall separating the two regions in the fluidized bed. This disturbs the system, resulting in unsteady values of D_{sr}. Nevertheless, the value of D_{sr} stabilizes after the system reaches a new pseudo-stationary condition. In Figure 2, we report the profiles of void-free mass fraction obtained from Eq. 5 and those obtained numerically at t = 5.0 s at the superficial gas velocity of 0.87 m/s (4.35 u_{mf}) for both 2D and 3D simulations. Similar profiles were obtained at other times and superficial

gas velocities. Figure 2 shows that the concentration varies in time faster in the 2D simulations. This happens for two reasons. The first is that in the 3D simulations the movement of the solid and the gas is restrained by the front and back walls. These are not accounted for in the 2D simulations. So, the lateral movement of the particles is slower in 3D simulations. This effect, however, is expected to be much reduced in large fluidized beds, in which wall effects are negligible. The second reason has to do with the dimensionality of the simulation and is always important. In 3D fluidized beds, the lateral motion of the solid has, we may say, two degrees of freedom, since the bubble-induced particle lateral motion develops on a horizontal plane. In 2D fluidized beds, in contrast, solely one degree of freedom is present, since the bubble-induced particle lateral motion can only develop along a horizontal line. This implies that lateral solid dispersion, and in turn the rate of change of the particle concentration, is overestimated in 2D fluidized beds (Norouzi et al., 2011). There is a good match between analytical and numerical profiles of void-free mass fraction reported in Figure 2, confirming that we can indeed employ Eq. 5 to model the lateral dispersion process.

The snapshots of solid-1 concentration are reported in Figures 3A and 3B, which refer to the 2D and 3D simulations, respectively, and to a superficial gas velocity of 0.87 m/s. The figures show how the tracer particles placed at the left of the removable partition wall spread to the right. We observe that the movement of solids in the 2D simulation is faster than that in the 3D simulation. This, as mentioned, is consistent with the profiles reported in Figure 2.

To investigate the role of frictional solid stress models on our numerical predictions, we ran the simulations considering the cases reported in Table 2, using the parameter and operational conditions reported in Table 1. The maximum particle packing was set to 0.63. This value is consistent with the maximum particle packing characterizing the DEM simulations. In these simulations, the particles are spherical and of equal size. For these kinds of system, the maximum packing usually has a density of about 63%. Song et al. (2008) predicted analytically that it cannot exceed a value of 63.4%. The restitution coefficient was set to 0.90, the same value used in the DEM simulations. Finally, the angle of internal friction was set to 30^{o} (the default value in Fluent 12.1). The sine of the angle of internal

friction features in the constitutive equation for the frictional solid viscosity (Schaeffer, 1987). The contribution of this term, however, is not dominant. For many powders the angle of internal friction ranges between 20 ^{o} and 40 ^{o}, so that the value of its sine is always unity. What dictate the order of magnitude of the frictional solid viscosity are the frictional solid pressure and the second invariant of the rate of deformation tensor.

We tested different frictional pressure and viscosity models, changing the solid volume fraction value at which the bed enters the frictional flow regime (ϕ_{min}) and observing the effects of such variations on lateral dispersion. Figure 4 (A-E) shows the variation of the lateral dispersion coefficient with superficial gas velocity for cases 1 to 5. The values of D_{sr} are compared with the empirical data of Shi & Fan (1984). We see that D_{sr} increases as the superficial gas velocity is increased. This is true for both 2D and 3D simulations, but, in all the cases considered, the 2D simulations clearly overestimate D_{sr}, the values being significantly higher than those given by the 3D simulations. The relative percentage errors for the 2D and 3D simulations are also reported in Figure 4 for all cases. Bègis & Balzer (1997) and Bègis et al. (1998) reported significant differences between the fluidization dynamics predicted by 2D and 3D simulations. To explain this, Xie et al. (2008) carried out a budget analysis of the governing differential equations, evaluating each term appearing in them. Their analysis revealed that the difference between the results of the 2D and 3D simulations is caused by the additional terms present in the three-dimensional equations of change. The difference, according to Xie et al. (2008), increases as the superficial gas velocity increases. This can explain why, in Figure 4, the difference between the 2D and 3D simulation results increases as the superficial gas velocity increases. Figure 4 reveals that, in all the cases investigated, the 3D results are reasonably good and agree with the empirical data better than the 2D results.

Figure 4 shows that the results of the 2D simulations are appreciably affected by the model used for the frictional solid stress (frictional pressure and frictional shear viscosity) and by the value ascribed to ϕ_{min}. The reasons for this were discussed in Oke et al. (2014) and so will not be repeated here. The results of the 3D simulations are far less sensitive to the frictional solid stress model. In both 2D and

3D simulations, we see that lowering the value of ϕ_{min} or using the constitutive model of Johnson & Jackson (1987) instead of the kinetic theory of granular flow (KTGF) model for the frictional pressure results into lower values of the lateral dispersion coefficient. As explained in Passalacqua & Marmo (2009) and in Oke et al. (2014), this is because the model of Johnson & Jackson (1987) yields larger solid pressure than the KTGF model, given the same solid concentration, whilst lowering the value of ϕ_{min} introduces this effect sooner, that is, at lower powder compaction. Larger solid pressures in turn result into smaller bubbles, reduced solid recirculation and reduced solid dispersion. This trend is also found in the 3D simulations, but the effect is less significant. For instance, for a fluid velocity of 1.17 m/s, the difference in the D_{sr} value between Cases 1 and 5 is 1.9 E-3 m^2/s for the 2D simulations, but reduces to 0.3 E-3 m^2/s for the 3D simulations.

From this study, we conclude that the simulation dimensionality plays the dominant role in predicting D_{sr} accurately. The frictional stress model does not seem to play as critical a role - as long as the third dimension is accounted for. The Eulerian-Eulerian models adopted in this work proved to be capable of predicting quite well the value of the lateral dispersion coefficient.

7.2 DEM simulations

This section investigates the capability of the Eulerian-Lagrangian modelling approach to estimate lateral dispersion coefficients; the intent is comparing its performance with that of Eulerian-Eulerian models. In the former approach, as stated, the closure problem for the frictional solid stress no longer arises, since we do not model the solid as a continuum.

We would like to point out that the powder and the bed geometry used in this second part of the work, which involves DEM simulations, are different from those considered in the CFD simulations above. This is because of the limitations imposed by the DEM modelling approach. The simulations needed to treat the same geometry and powder considered in the CFD simulations are far too expensive for our computational resources, requiring about 13 million more particles than those used in the DEM simulations that we were able to run. Because our aim is comparing the performance of the Eulerian-

Eulerian and Eulerian-Lagrangian modelling approaches, we simulated a new geometry and powder. We studied the powder investigated experimentally by Grakhovskii (1968), which has a bigger mean size than that employed previously. The parameters used in our simulations, in particular the bed height and the superficial gas velocities, were chosen to replicate the work of the author. Nevertheless, the depth and the width of the bed used in our simulations are smaller than those of Grakhovskii (he used a bed of depth 100 mm and width 1000 mm). This is, once again, because of the huge computational cost we would have incurred if we had employed the real dimensions of the bed investigated by Grakhovskii. In Table 3, we summarize the powder properties and the bed dimensions employed in our simulations.

To estimate the D_{sr} values, we used the same procedure as in the Eulerian-Eulerian simulations. The results of DEM simulations provide the position of each particle at any given time. This allowed us to determine the radial void-free concentration profiles in the bed. By matching these profiles with those obtained analytically from Eq. 5, we calculated the D_{sr} values at different operational conditions. We report in Figure 5 the concentration profiles for a superficial gas velocity of 1.9 m/s; the values of the other parameters are those shown in Table 3. The profile given by the 3D CFD simulation is also included for completeness. We observe a good match between the numerical and analytical profiles. These refer to a time $t = 2.0\ s$, but similar results were obtained at other times and superficial gas velocities. Figure 5 suggests that mixing is slower in DEM simulations. The reason for this is closely linked to the values assigned to the collision parameters. We will discuss this aspect in the following paragraphs.

We should note that the accuracy of the simulations depends on the values assigned to the parameters appearing in the model (i.e., *restitution coefficient*, *particle-particle friction coefficient* and *stiffness constant*); therefore, care has to be taken when choosing them. The coefficient of restitution accounts for the kinetic energy dissipated when particles collide. The energy that is lost is accounted for by the contact damping force included in the DEM model through the dashpot model. It is customary to base the damping coefficient on the collisional properties of the particles, in particular the restitution

coefficient e. Nevertheless, we should note that the latter is neither a material property nor a constant. Its value depends, among other parameters, on the relative impact velocity of the colliding particles (Kuwabara & Kono, 1987). However, the variation of the restitution coefficient is negligible, except at very high impact velocities (usually 10 m/s and above) (Labous et al., 1997). So, the value of e is normally taken to be constant in DEM simulations. The typical value employed in the literature is 0.90, and therefore in this work we employed this value (which was also used in the Eulerian-Eulerian simulations). Unlike the coefficient of restitution, the friction coefficient and the material stiffness constants depend on the material properties. The friction coefficient is an empirical parameter whose value depends on many factors, including particle shape, particle size and surface texture, whilst the material stiffness constants depend on the Young's modulus and Poisson's ratio of the material. Since we do not have the empirical values for these parameters (even if we did, we could not have used them, because the simulations would have been too computationally expensive), we performed a parametric study to determine how the values assigned to them influence the simulation results.

To see how friction coefficient and stiffness affect the numerical predictions of D_{sr}, we carried out a sensitivity analysis on them using the values of parameters reported in Table 3 as a reference case. We began by considering the effect of the friction coefficient. This parameter may affect significantly the fluidized bed dynamics in DEM simulations. Cleary et al. (1998) carried out a sensitivity analysis on it, studying the effect that its value has on the solid mixing rates in a ball mill. They reported that the mixing rate increased as the friction coefficient decreased. To investigate the influence of the friction coefficient on lateral solid mixing, we performed simulations using different values of μ in the range commonly used in DEM simulations of fluidized beds, keeping the restitution coefficient at 0.90, the superficial gas velocity at 2.66 m/s (3.5 umf – an intermediate value in the velocity range investigated experimentally by Grakhovskii) and the normal material stiffness constant K_n at 40,977 N/m$^{3/2}$. The value of K_n was obtained via Eq. 22. The snapshots of the bed, obtained using the reference conditions in Table 3 at a superficial gas velocity of 2.66 m/s, at different computational times, are reported in Figure 6. The latter shows the lateral spread of particles. This is similar to what we

observed in the CFD simulations described in the previous section. Figure 7 shows that D_{sr} reduces as the friction coefficient increases. This is consistent with the findings of Cleary et al. (1998) and was expected. When the friction coefficient rises, the sustained particle-particle interactions become more pronounced and the gross particle circulation in the bed (induced by the bubbles) is curtailed. This results in a reduction of the dispersion coefficient. Its order of magnitude, however, remains the same. The results of the simulations did not evidence a marked effect of the friction coefficient value on the bubbling behaviour of the bed.

Generally, the value of material stiffness constants should as well be carefully chosen, since it affects the integration time step significantly: the higher the stiffness, the smaller the necessary integration time step. This is because higher stiffness results in shorter collision times. Stiffness also influences interparticle overlap during collisions; generally, small stiffness leads to large interparticle overlap. Stiffness values must be chosen in such a way as to attain a balance between accuracy and computational efficiency. A large stiffness value, even if it may yield more accurate results, does reduce the computational efficiency dramatically. On the other hand, when stiffness values are impractically small, the accuracy of the simulations could be compromised. Therefore, it requires careful judgement on the modeller's part to strike a reasonable balance between accuracy and efficiency. To investigate the effect of material stiffness on the lateral dispersion coefficient, we conducted a sensitivity analysis on it, using the parameters reported in Table 3 as a reference case. We ran simulations at different stiffness values, keeping the coefficient of restitution at 0.90, the friction coefficient at 0.20 and the superficial gas velocity at 2.66 m/s. Figure 8 reports how D_{sr} changes with stiffness. We can see that D_{sr} decreases slowly initially, and then more rapidly, as stiffness increases. However, the order of magnitude of D_{sr} remains unchanged. Also in this case we observed that, for the range of values considered, the stiffness constant did not affect markedly the bubbling behaviour of the bed.

We investigated how the bed thickness (i.e. the bed depth in the z-direction) influences the D_{sr} values, because we could not simulate directly the experimental system, adopting the real value of bed depth

(100 mm), owing to the enormous computational resources required. Hence, we decided to investigate how the choice of bed depth value affects the numerical prediction of $D_{sr.}$ In the literature, the effect of the bed thickness has mainly been studied with respect to the minimum fluidization velocity. It was observed that the latter increases as the bed thickness decreases (Caicedo et al., 2002; Kathuria & Saxena, 1987; Sanchez-Delgado et al., 2011; Saxena & Vadivel, 1988). This is because, as the bed depth reduces, the effect of wall friction becomes more pronounced, limiting the movement of the particles. For this same reason, we believed that the bed thickness would affect our numerical results. Indeed, studies have shown that bed thickness does affect bubble size, shape, velocity and expansion; these are important parameters that strongly influence solid mixing in fluid beds (Cranfield & Geldart, 1974; Geldart, 1970; Geldart & Cranfield, 1972; Glicksman & McAndrews, 1985; Rowe & Everett, 1972). To investigate the effect of bed thickness, we ran simulations at different superficial fluid velocities, using geometries of depths $10\ dp$ and $20\ dp$, where dp is the particle diameter, and (in a third case) periodic walls at $10\ \ dp$ (imposing periodic boundary conditions at the front and back walls of the vessel). The values of the simulation parameters were those shown in Table 3. Figure 9 reports how D_{sr} changes with the superficial gas velocity for the various bed depths examined. We note that D_{sr} reduces as the depth of the bed is decreased, as expected. The simulations run with periodic boundary condition give higher values of D_{sr} than those with rigid walls, because the walls do not constrain the bed dynamics. Since the depth of the bed considerably affects solid dispersion, in the simulations one should employ the correct dimension (the same as that of the real system investigated experimentally). If doing so is not feasible (for instance because the number of particles to be tracked would be too large), then one has to keep in mind that simulating a narrower bed may affect the simulation results, leading to lower dispersion coefficient values, as seen in Figure 9.

The results presented in these paragraphs reveal that DEM simulations are able to estimate the rate of lateral solid mixing in fluidized beds, but the accuracy of this modelling approach, as we have seen, depends on the values chosen for the simulation parameters. So, even if we are not faced with the problem of constitutively expressing the frictional solid stress, as we are in the Eulerian-Eulerian

simulations, we are still faced with the challenge of assigning appropriate values to the simulation parameters. To overcome this issue, one needs to estimate the parameters experimentally, but doing so is extremely time-consuming, and, as pointed out before, employing the empirical values in the simulations would require enormous computational resources; this, in particular, is true for the material stiffness constants. In the next section, we compare the DEM simulation results with the experimental ones and with those obtained from the Eulerian-Eulerian simulations.

7.3 DEM versus CFD simulations

We ran simulations in CFD using the same powder, geometry and operational conditions employed in the DEM simulations. Table 4 reports the simulation parameters and the powder properties used in the CFD simulations. In the DEM ones, we considered two stiffness values: 40,977 N/m$^{3/2}$ and 409,772 N/m$^{3/2}$. For each, we ran simulations at various superficial gas velocities, keeping the other parameters constant (the values are those reported in Table 3). Figure 10 reports how D_{sr} changes with superficial gas velocity. We observe that D_{sr} increases with superficial gas velocity; this is expected because an increase in the latter induces more bubbling, which makes the rate of lateral solid mixing rise. The D_{sr} values calculated at 40,977 N/m$^{3/2}$ are larger than those calculated at 409,772 N/m$^{3/2}$. This is true for all the superficial gas velocities considered and agrees with what Figure 8 reports.

In the CFD simulations we considered Cases 1 and 5 reported in Table 2. The void-free mass fraction profile for Case 1 obtained at a superficial gas velocity of 1.9 m/s is reported in Figure 5. In Figure 10, it is interesting to note that the D_{sr} values obtained in Case 5 are lower than those obtained in Case 1. The trend is the same as that observed in the previous CFD simulations reported above. The figure also shows that the CFD simulations predict the D_{sr} values better than the DEM simulations, although the empirical data are still slightly overestimated. The predictions of the DEM simulations are fairly accurate, the order of magnitude of the results matching that of the empirical data. This reveals that DEM simulations are equally capable of estimating D_{sr} accurately, provided one assigns appropriate values to the collision parameters.

8.0 Conclusions

In this article, we extended our previous work on the numerical simulations of lateral solid mixing in gas-fluidized beds (Oke et al., 2014). In the latter, our numerical results overestimated the empirical ones. We attributed this to the 2D nature of our simulations and to the frictional stress models used. In this paper we addressed these problems. We examined the influence of simulation dimensionality. We ran CFD simulations in 3D at different superficial gas velocities, considering the same powder and the same geometry as those employed in our 2D simulations. Our results showed that the 3D simulations predict D_{sr} better. We also noticed that the effects of frictional stress models, while still present in the 3D simulations, are less significant than in the 2D simulations. Hence, we concluded that simulation dimensionality plays the dominant role in the overestimation of D_{sr}. After, we tested the capability of DEM simulations to predict D_{sr}. The DEM results agreed reasonably well with empirical results. The simulation results revealed that the accuracy of numerical predictions depends on the values assigned to the collision parameters; in particular, the restitution coefficients, friction coefficients and stiffness. To conclude, we compared the results obtained from the DEM (i.e. Eulerian-Lagrangian) and the CFD (i.e., Eulerian-Eulerian) simulations. We observed that both modelling approaches predicted D_{sr} fairly accurately. Nevertheless, CFD simulations yielded slightly better results.

References

Avidan, A., Yerushalmi, J., 1985. Solids mixing in an expanded top fluid bed. American Institute of Chemical Engineers, 31, 835-841.

Bellgardt, D., Schoessler, M., Werther, J. 1985. An investigation into the lateral mixing of feed particles in atmospheric fluidized-bed combustors. International Conference on Fluidized-Bed Combustion,115-129.

Bégis, J., Balzer, G. 1997. Modélisation numérique 2D et 3D de lit fluidisé circulant: application a la réalisation du diagramme des régimes. Tech. Rep. HE/44/97/001A.

Bégis, J., Flour, I., Peirano, E. 1998. Modélisation numérique d'un distributeur d'air appliqué aux lits fluidises de l'Universitae de Chalmers. Tech. Rep. HE/44/98/017/A.

Borodulya, V. A., Epanov, Y. G., Teplitskii, Y. S.1982. Horizontal particle mixing in a free fluidized bed. Journal of Engineering Physics, 42, 528-533.

Chirone, R., Miccio, F., Scala, F. 2004. On the relevance of axial and transversal fuel segregation during the FB combustion of a biomass. Energy and Fuels, 18, 1108-1117.

Caicedo, G. R., Ruiz, M. G., Marques, J. J. P., Soler, J. G. 2002. Minimum fluidization velocities for gas-solid 2D beds. Chemical Engineering and Processing, 41, 761-764.

Cleary, P. W., Metcalfe, G., Liffman, K. 1998. How well do discrete element granular flow models capture the essentials of mixing processes? Applied Mathematical Modelling, 22, 995-1008.

Cranfield, R. R., Geldart, D. 1974. Large particle fluidisation. Chemical Engineering Science, 29, 935-947.

Cundall, P. A., Strack, O. D. L. 1979. A discrete numerical model for granular assemblies. Geotechnique, *29*, 47-65.

Di Renzo, A., Di Maio, F. P. 2004. Comparison of contact-force models for the simulation of collisions in DEM-based granular flow codes. Chemical Engineering Science, 59, 525-541.

Farzaneh, M., Sasic, S., Almstedt, A., Johnsson, F., Pallarès, D. 2011. A novel multigrid technique for lagrangian modeling of fuel mixing in fluidized beds. Chemical Engineering Science, 66, 5628-5637.

Gera, D., Gautam, M., Tsuji, Y., Kawaguchi, T., Tanaka, T. 1998. Computer simulation of bubbles in large-particle fluidized beds. Powder Technology, 98, 38-47.

Grace, J. R. 1981. Fluidized bed reactor modeling: an overview. ACS Symp. Ser., 168, 3-18.

Geldart, D. 1970. The size and frequency of bubbles in two- and three-dimensional gas-fluidised beds. Powder Technology, 4, 41-55.

Geldart, D., Cranfield, R. R. 1972. The gas fluidization of large particles. Chemical Engineering Journal, 3, 211-231.

Glicksman, L. R., McAndrews, G. 1985. The effect of bed width on the hydrodynamics of large particle fluidized beds. Powder Technology, 42, 159-167.

Grakhovskii, B. M. 1968. Particle mixing and residence time in a fluidized bed: High temperature endothermal processes in a fluidized bed (in Russian), Metallurgiya, Moscow, 70-75.Mosc

Hirama, T., Ishida, M., Shirai, T. 1975. The lateral dispersion of solid particles in fluidized beds. Kagaku Kogaku Ronbunshu,1, 272-276.

Johnson K. L. Contact Mechanics. Cambridge university press. 1987.

Johnson, P. C., Jackson, R., 1987. Frictional-collisional constitutive relations for granular materials, with application to plane shearing. Journal of Fluid Mechanics, 176, 76-93.

Kaneko, Y., Shiojima, T., Horio, M. 1999. DEM simulation of fluidized beds for gas-phase olefin polymerization. Chemical Engineering Science, 54, 5809-5821.

Kathuria, D. G., Saxena, S. C. 1987. A variable-thickness two-dimensional bed for investigating gas-solid fluidized bed hydrodynamics. Powder Technology, 53, 91-96.

Kawaguchi, T., Tanaka, T., Tsuji, Y. 1998. Numerical simulation of two-dimensional fluidized beds using the discrete element method (comparison between the two- and the three-dimensional models). Powder Technology, 96, 129-138.

Kuwabara, G., Kono, K. 1987. Restitution coefficient in a collision between 2 spheres. Japanese Journal of Applied Physics, *26*, 1230-1233.

Labous, L., Rosato, A. D., Dave, R. N. 1997. Measurements of collisional properties of spheres using high-speed video analysis. Physical Review, *56*, 5717–5725.

Lettieri, P., Mazzei, L. 2009. Challenges and issues on the CFD modeling of fluidized beds: A review. Journal of Computational Multiphase Flows, 1, 83-131.

Lewis, W. K., Gilliland, E. R., Girouard, H., 1962. Heat transfer and solids mixing in a bed of fluidized solids. Chemical Engineering Progress Symposium, 58, 87-97.

Lim, K. S., Agarwal, P. K. 1994. Circulatory motion of a large and lighter sphere in a bubbling fluidized bed of smaller and heavier particles. Chemical Engineering Science, 49, 421-424.

Liu, D., Chen, X. 2010. Lateral solid dispersion in large scale fluidized beds. Combustion and Flame, 157, 2116-2124.

Lo, S. M. 1989. Mathematical basis of a multiphase flow model, AERE R 13432.

Mallouppas, G., van Wachem, B. G. M. 2013. Large eddy simulations of turbulent particle-laden channel flow. International Journal of Multiphase Flow, 54, 65-75.

May, W. G., 1956. Fluidized bed reactor studies. Chemical Engineering Progress, 55, 49-56.

Mazzei, L., Lettieri, P., 2007. A drag force closure for uniformly-dispersed fluidized suspensions. Chemical Engineering Science, 62, 6129-6142.

Mikami, T., Kamiya, H., Horio, M. 1998. Numerical simulation of cohesive powder behaviour in a fluidized bed. Chemical Engineering Science, 53, 1927-1940.

Mindlin, R. D. 1949. Compliance of elastic bodies in contact. Journal of Applied Mechanics, 16, 259-268.

Mindlin, R. D., Deresiewicz, H. 1953. Elastic spheres in contact under varying oblique forces. Journal of Applied Mechanics, 75, 327-344.

Norouzi, H. R., Mostoufi, N., Mansourpour, Z., Sotudeh-Gharebagh, R., Chaouki, J. 2011. Characterization of solids mixing patterns in bubbling fluidized beds. Chemical Engineering Research and Design, 89, 817-826.

Oke, O., Lettieri, P., Solimene, R., Salatino, P., Mazzei, L. 2014. Numerical simulations of lateral solid mixing in gas fluidized beds. Chemical Engineering Science, 120, 117-129.

Oke, O., Lettieri, P., Salatino, P., Solimene, R., Mazzei, L. 2015. Eulerian modeling of lateral solid mixing in gas-fluidized suspensions. Procedia Engineering, 102, 1491-1499.

Pallarès, D., Johnsson, F. 2006. A novel technique for particle tracking in cold 2-dimensional fluidized beds – simulating fuel dispersion. Chemical Engineering Science, 61, 2710-2720.

Pallarès, D., Diez, P., Johnsson, F. 2007. Experimental analysis of fuel mixing patterns in a fluidized bed. 12th International Conference on Fluidization, Vancouver, Canada, 929-936.

Passalacqua, A., Marmo, L., 2009. A critical comparison of frictional stress models applied to the simulation of bubbling fluidized beds. Chemical Engineering Science, 160, 2795-2806.

Rhodes, M. J., Wang, X. S., Nguyen, M., Stewart, P., Liffman, K. 2001. Use of discrete element method simulation in studying fluidization characteristics: influence of interparticle force. Chemical Engineering Science, 56, 69-76.

Rong, D. G., Mikami, T., Horio, M. 1999. Particle and bubble movements around tubes immersed in fluidized beds – a numerical study. Chemical Engineering Science, 54, 5737-5754.

Rowe, P. N., Everett, D. J. 1972. Fluidised bed bubbles viewed by X-rays Part II – The transition from two to three dimensions of undisturbed bubbles. Chemical Engineering Research and Design, 50, 49-54.

Salam, T. F., Ren, Y., Gibbs, B. M. 1987. Lateral solid and thermal dispersion in fluidized bed combustors. Proceedings of international Conference on Fluid Bed Combustion, 9, 541.

Saxena, S. C., Vadivel, R. 1988. Wall effects in gas-fluidized beds at incipient fluidization. Chemical Engineering Journal, 39, 133-137.

Sanchez-Delgado, S., Almendros-Ibanez, J. A., Garcia-Hernando, N., Santana, D. 2011. On the minimum fluidization velocity in 2D fluidized beds. Powder Technology, 207, 145-153.

Schaeffer, D. G., 1987. Instability in evolutions describing incompressible granular flow. Journal of Differential Equations, 66, 19-50.

Shi, Y., Fan, L. T. 1984. Lateral mixing of solids in batch gas-solid fluidized beds. Industrial & Engineering Chemistry Process Design and Development, 23, 337-341.

Song, C., Wang, P., Makse, H. A. 2008. A phase diagram for jammed matter. Nature, 453, 629-632.

Tagliaferri, C., Mazzei, L., Lettieri, P., Marzocchella, A., Olivieri, G., Salatino, P. 2013. CFD simulation of bubbling fluidized bidisperse mixtures: Effect of integration methods and restitution coefficient. Chemical Engineering Science, 102, 324-334.

Tian, F., Zhang, M., Fan, H., Gu, M., Wang, L., Qi, Y. 2007. Numerical studies on microscopic mixing characteristics in fluidized beds via DEM. Fuel Processing Technology, 88, 187-198.

Tsuji, Y., Tanaka, T., & Ishida, T. 1992. Lagrangian numerical-simulation of plug flow of cohesionless particles in a horizontal pipe. Powder Technology, *71*, 239–250.

van der Hoef, M. A., van Sint Annaland, M., Deen, N. G., Kuipers, J. A. M. 2008. Numerical simulation of dense gas-solid fluidized beds: A multiscale modeling strategy, 40, 47-70.

van Wachem, B. G. M., Almstedt, A. 2003. Methods for multiphase computational fluid dynamics. Chemical Engineering Journal, 96, 81-98.

van Wachem, B., Benavides, A., Gopala, V. 2007. A coupled solver approach for multiphase flow problems. In: 6th International Conference on Multiphase Flows 2007, Leipzig, Germany

van Wachem, B. G. M., Yu. X., Hsu, T. 2010. A 3D Eulerian-Lagrangian numerical model for sediment transport. 7th International Conference on Multiphase Flow. ICMF. Vol. 2010.

van Wachem, B. G. M., Zastawny, M., Zhao, F., Mallouppas, G. 2015. Modelling of gas-solid turbulent channel flow with non-spherical particles with large stokes numbers. International Journal of Multiphase Flow, 68, 80-92.

Xiang, Q., Huang, G., Ni, M., Cen, K., Tao, T. 1987. Lateral dispersion of large coal particles in an industrial-scale fluidized. Proceedings of International Conference on Fluid Bed Combustion, 9, 546.

Xiao P., Yan, G., Wang, D. 1998. Investigation on horizontal mixing of particles in dense bed in circulating fluidized bed (CFB). Journal of Thermal Science,7, 78-84.

Xie, N., Battaglia, F., Pannala, S. 2008. Effects of using two- versus three-dimensional computational modeling of fluidized beds: Part II, budget analysis. Powder Technology, 182, 14-24.

Figure 1

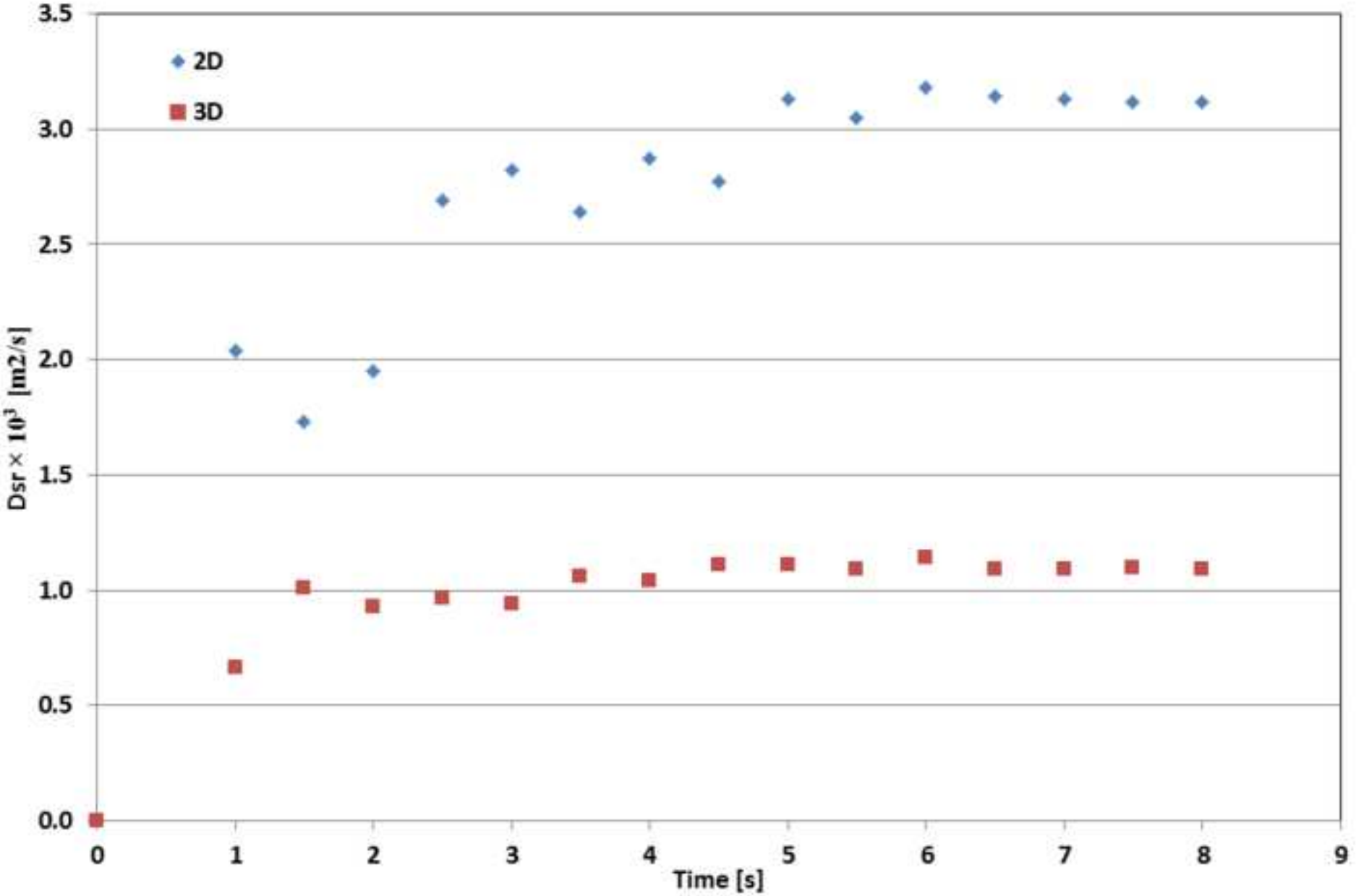

Figure 2

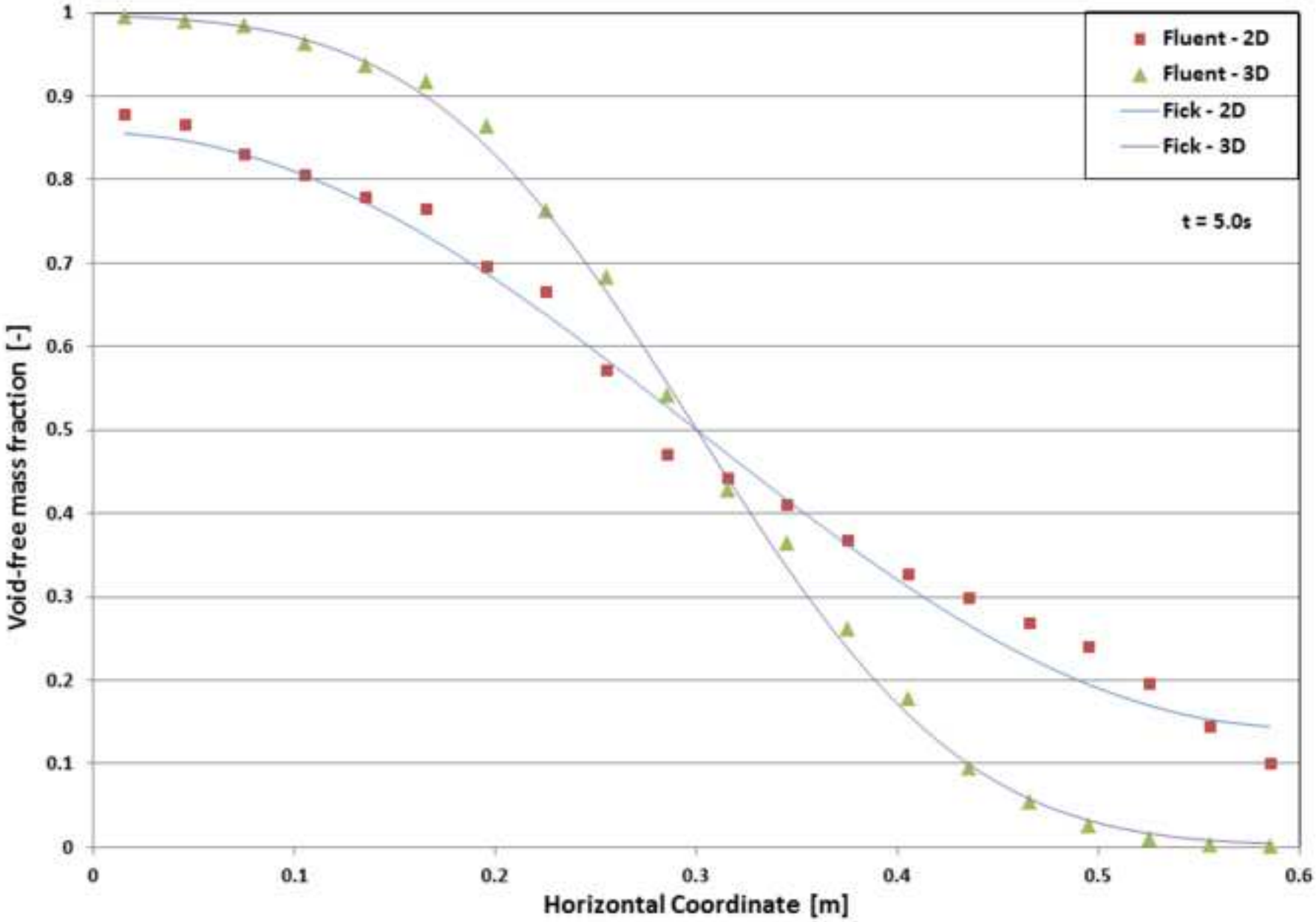
Fluent - 2D
Fluent - 3D
Fick - 2D
Fick - 3D
t = 5.0s
Void-free mass fraction [-]
Horizontal Coordinate [m]
0
0.1
0.2
0.3
0.4
0.5
0.6
0.7
0.8
0.9
1

Figure 3

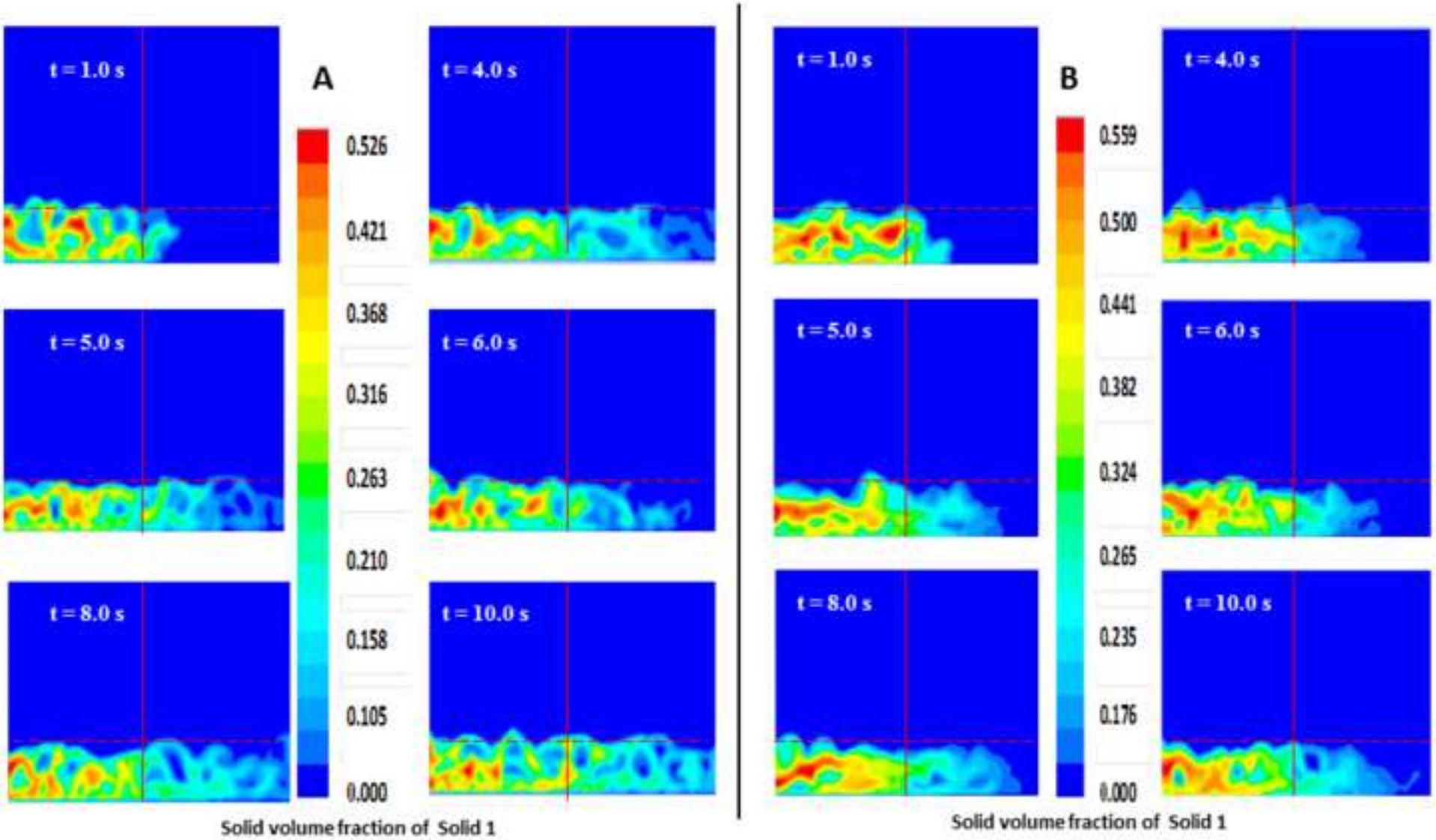
A
t = 1.0 s
t = 4.0 s
t = 5.0 s
t = 6.0 s
t = 8.0 s
t = 10.0 s
0.526
0.421
0.368
0.316
0.263
0.210
0.158
0.105
0.000
Solid volume fraction of Solid 1
B
t = 1.0 s
t = 4.0 s
t = 5.0 s
t = 6.0 s
t = 8.0 s
t = 10.0 s
0.559
0.500
0.441
0.382
0.324
0.265
0.235
0.176
0.000
Solid volume fraction of Solid 1

Figure 4A

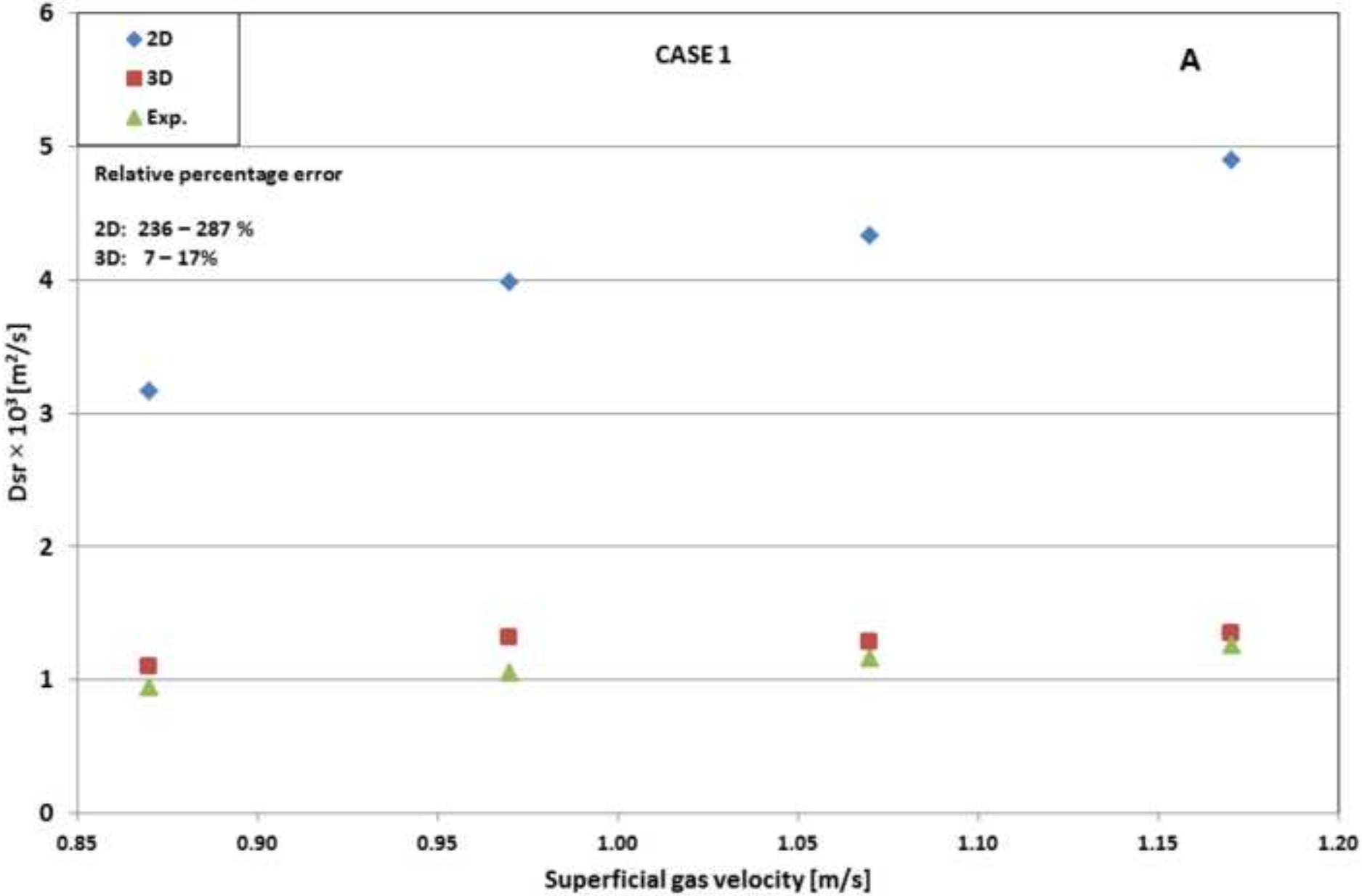
2D
3D
Exp.
CASE 1
A
Relative percentage error
2D: 236 – 287 %
3D: 7 – 17%
Dsr × 10³ [m²/s]
Superficial gas velocity [m/s]
0
1
2
3
4
5
6
0.85
0.90
0.95
1.00
1.05
1.10
1.15
1.20

Figure 4B

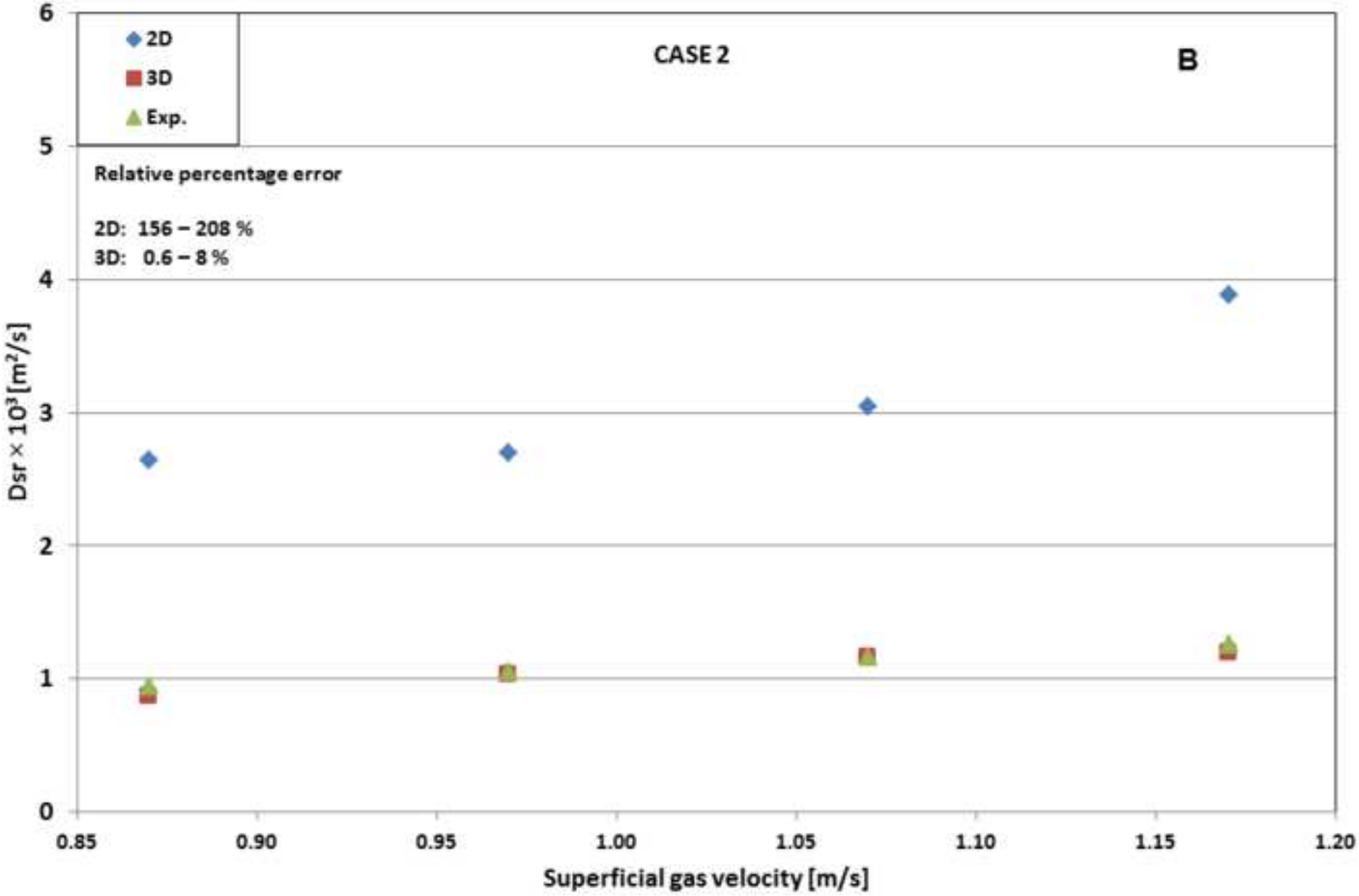
2D
3D
Exp.
CASE 2
B
Relative percentage error
2D: 156 – 208 %
3D: 0.6 – 8 %
Dsr × 10³ [m²/s]
Superficial gas velocity [m/s]
0
1
2
3
4
5
6
0.85
0.90
0.95
1.00
1.05
1.10
1.15
1.20

Figure 4C

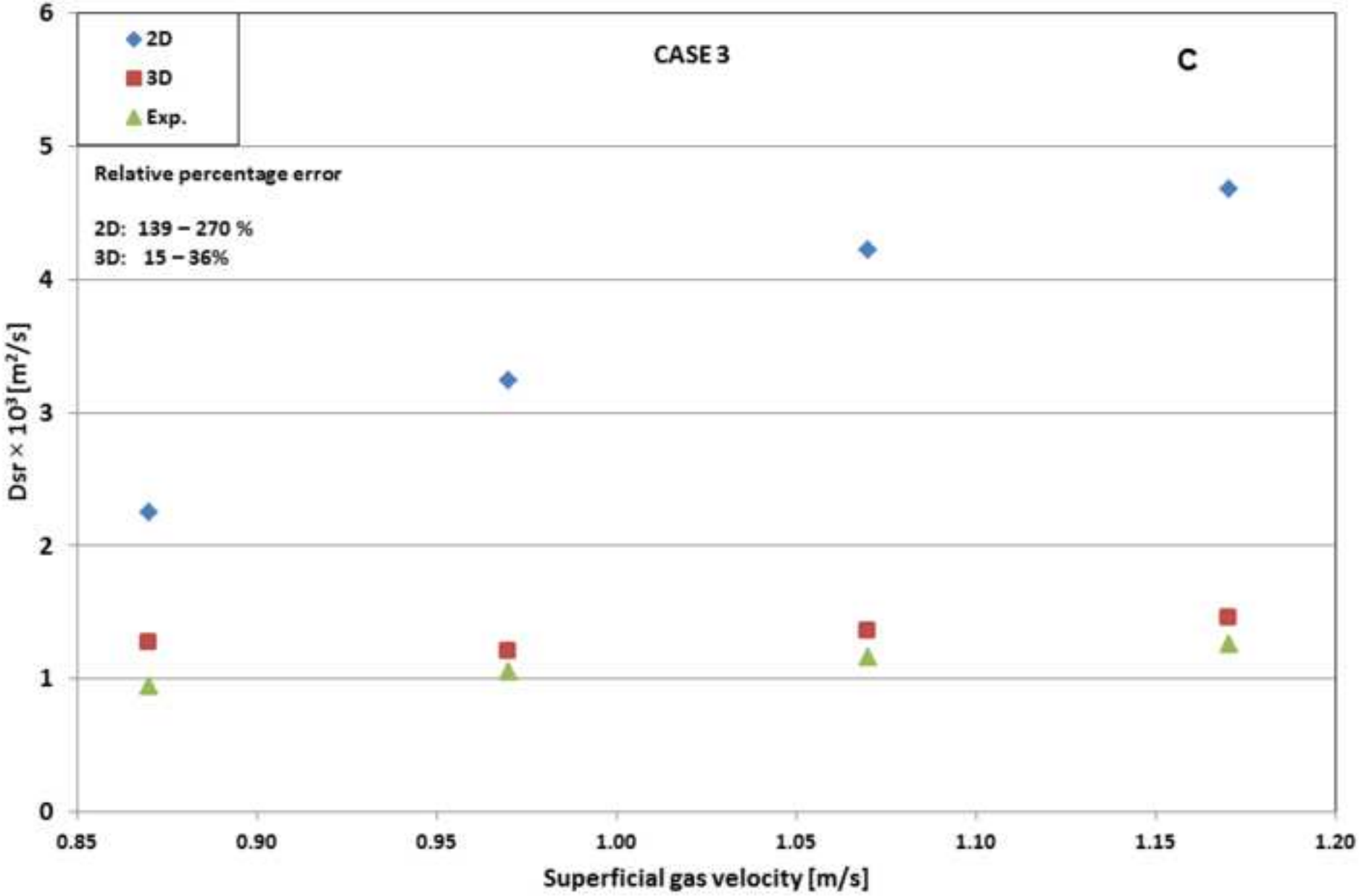
2D
3D
Exp.
CASE 3
C
Relative percentage error
2D: 139 – 270 %
3D: 15 – 36%
Dsr × 10³ [m²/s]
Superficial gas velocity [m/s]
0
1
2
3
4
5
6
0.85
0.90
0.95
1.00
1.05
1.10
1.15
1.20

Figure 4D

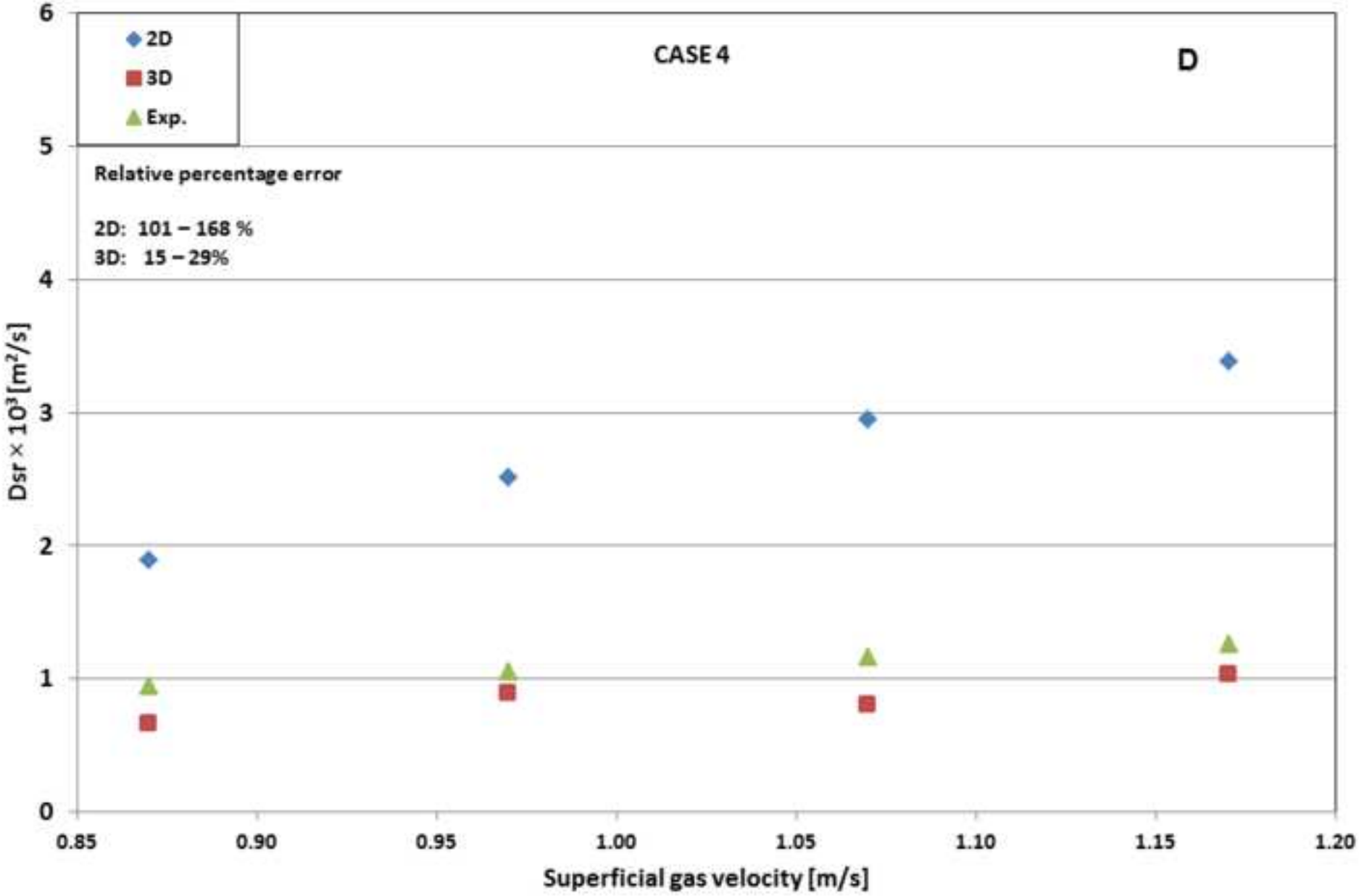
2D
3D
Exp.
CASE 4
D
Relative percentage error
2D: 101 – 168 %
3D: 15 – 29%
Dsr × 10³ [m²/s]
Superficial gas velocity [m/s]
0
1
2
3
4
5
6
0.85
0.90
0.95
1.00
1.05
1.10
1.15
1.20

Figure 4E

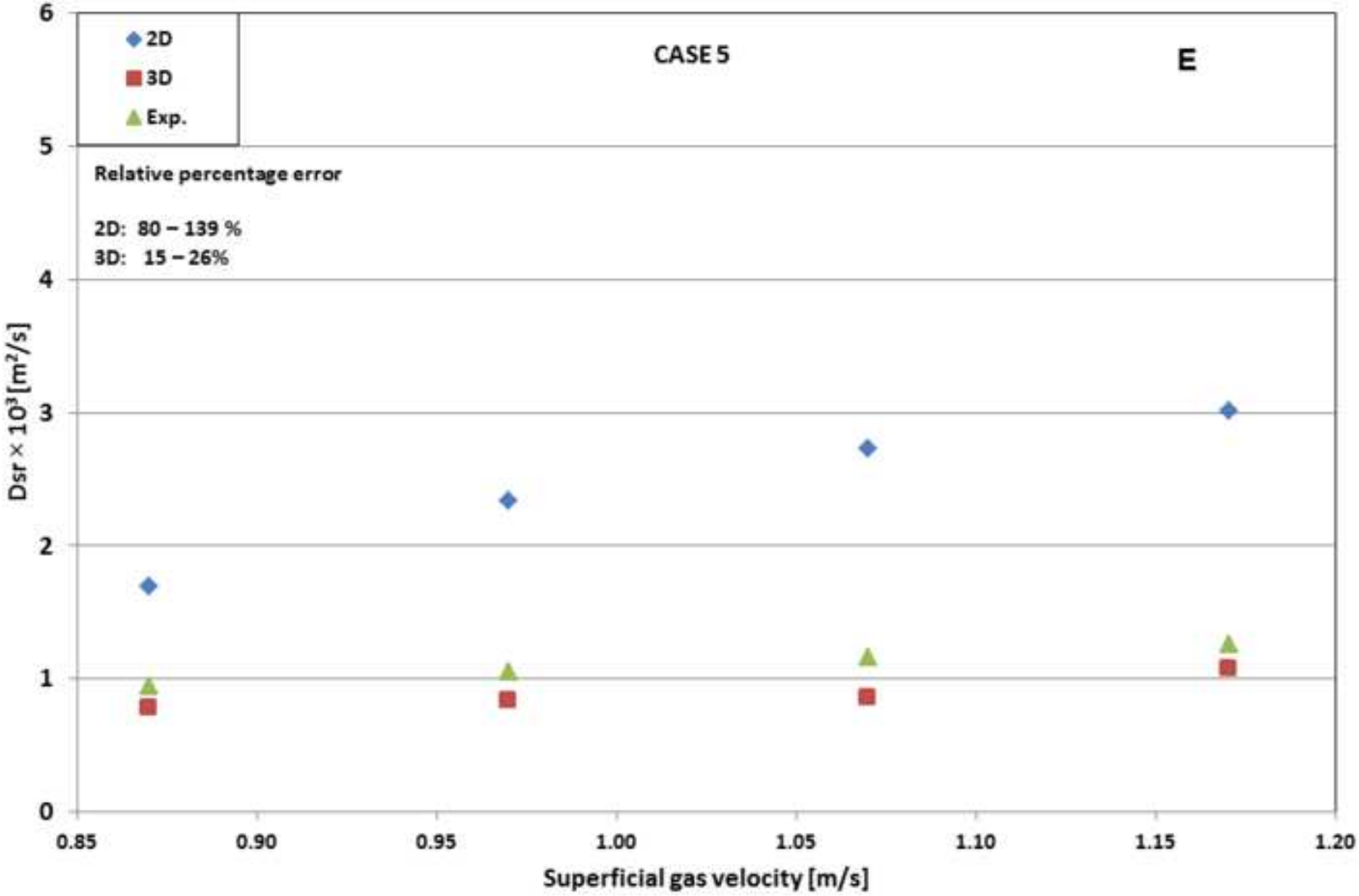
2D
3D
Exp.
CASE 5
E
Relative percentage error
2D: 80 – 139 %
3D: 15 – 26%
Dsr × 10³ [m²/s]
Superficial gas velocity [m/s]
0
1
2
3
4
5
6
0.85
0.90
0.95
1.00
1.05
1.10
1.15
1.20

Figure 5

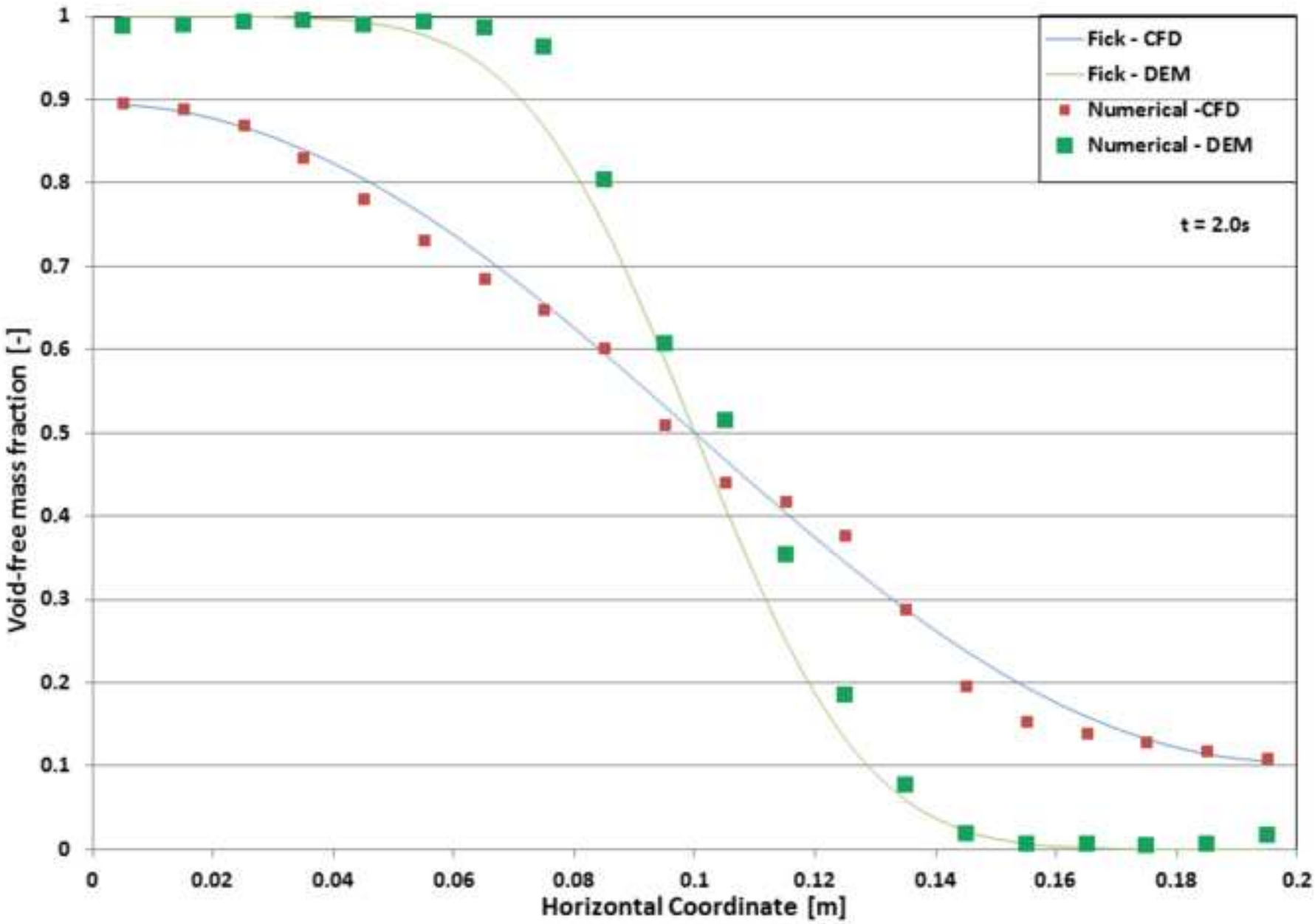
Fick - CFD
Fick - DEM
Numerical -CFD
Numerical - DEM
t = 2.0s
Void-free mass fraction [-]
Horizontal Coordinate [m]
0
0.1
0.2
0.3
0.4
0.5
0.6
0.7
0.8
0.9
1
0
0.02
0.04
0.06
0.08
0.1
0.12
0.14
0.16
0.18
0.2

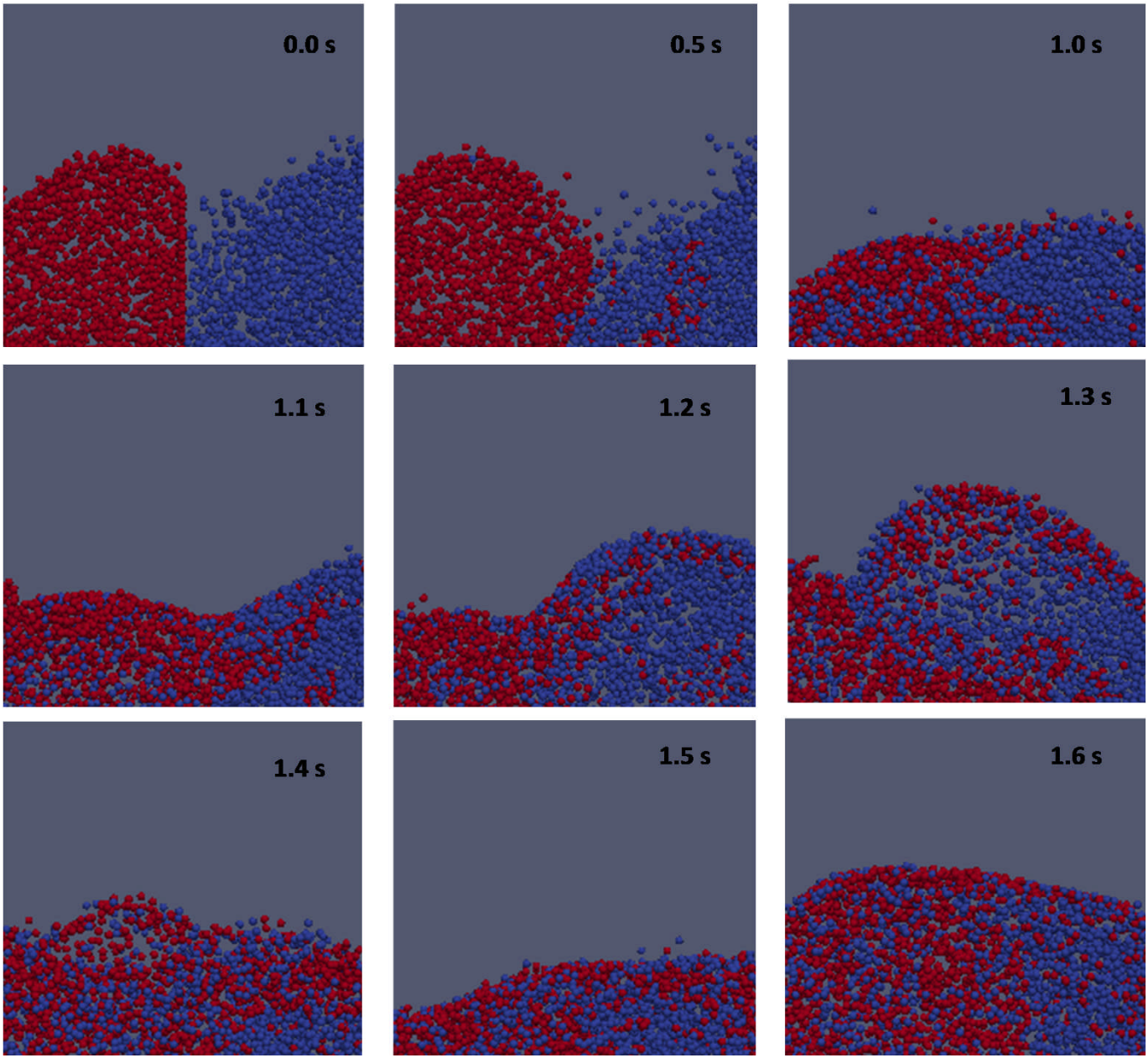
0.0 s
0.5 s
1.0 s
1.1 s
1.2 s
1.3 s
1.4 s
1.5 s
1.6 s

Figure 7

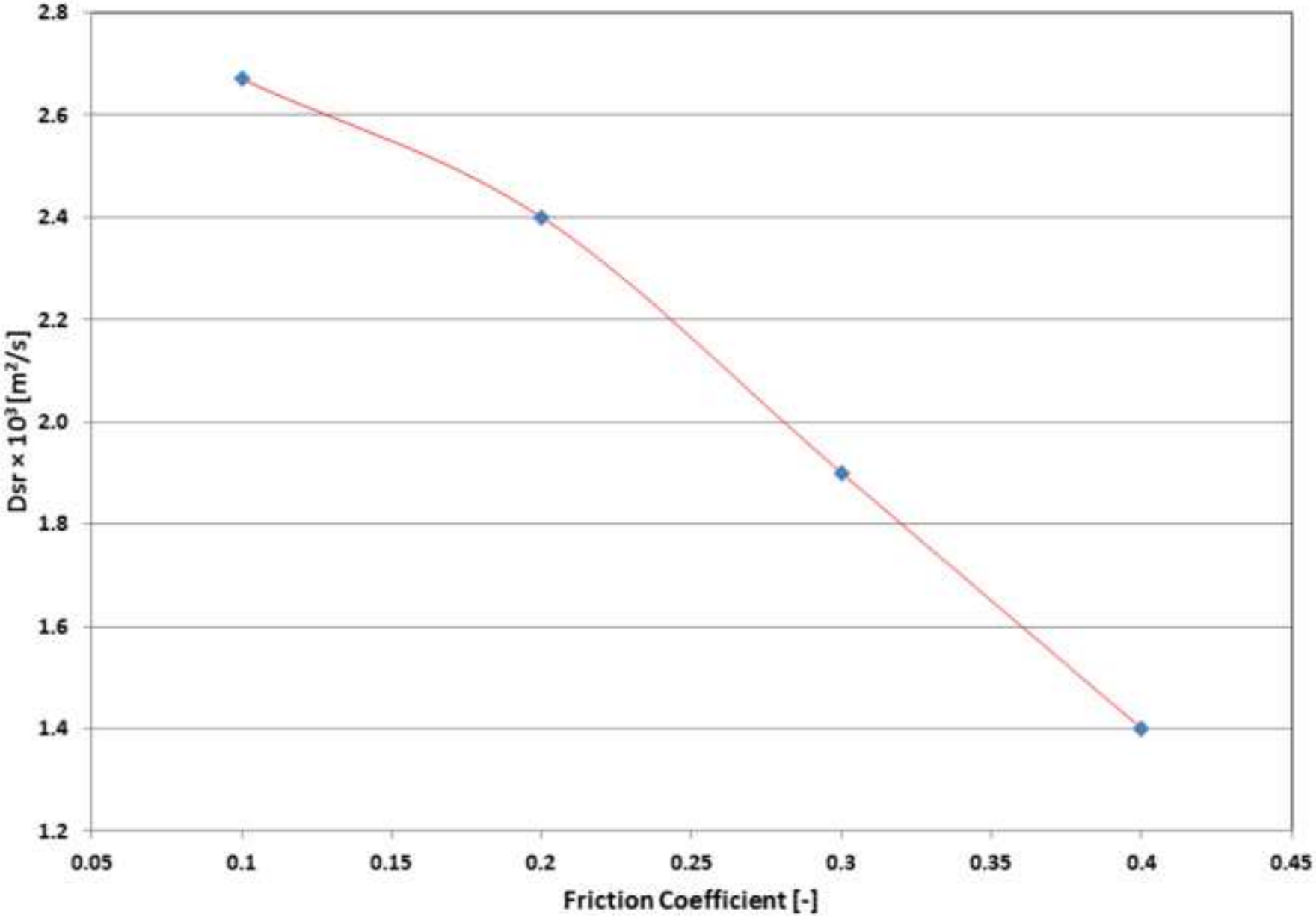
2.8
2.6
2.4
2.2
2.0
1.8
1.6
1.4
1.2
Dsr × 10³ [m²/s]
0.05
0.1
0.15
0.2
0.25
0.3
0.35
0.4
0.45
Friction Coefficient [-]

Figure 8

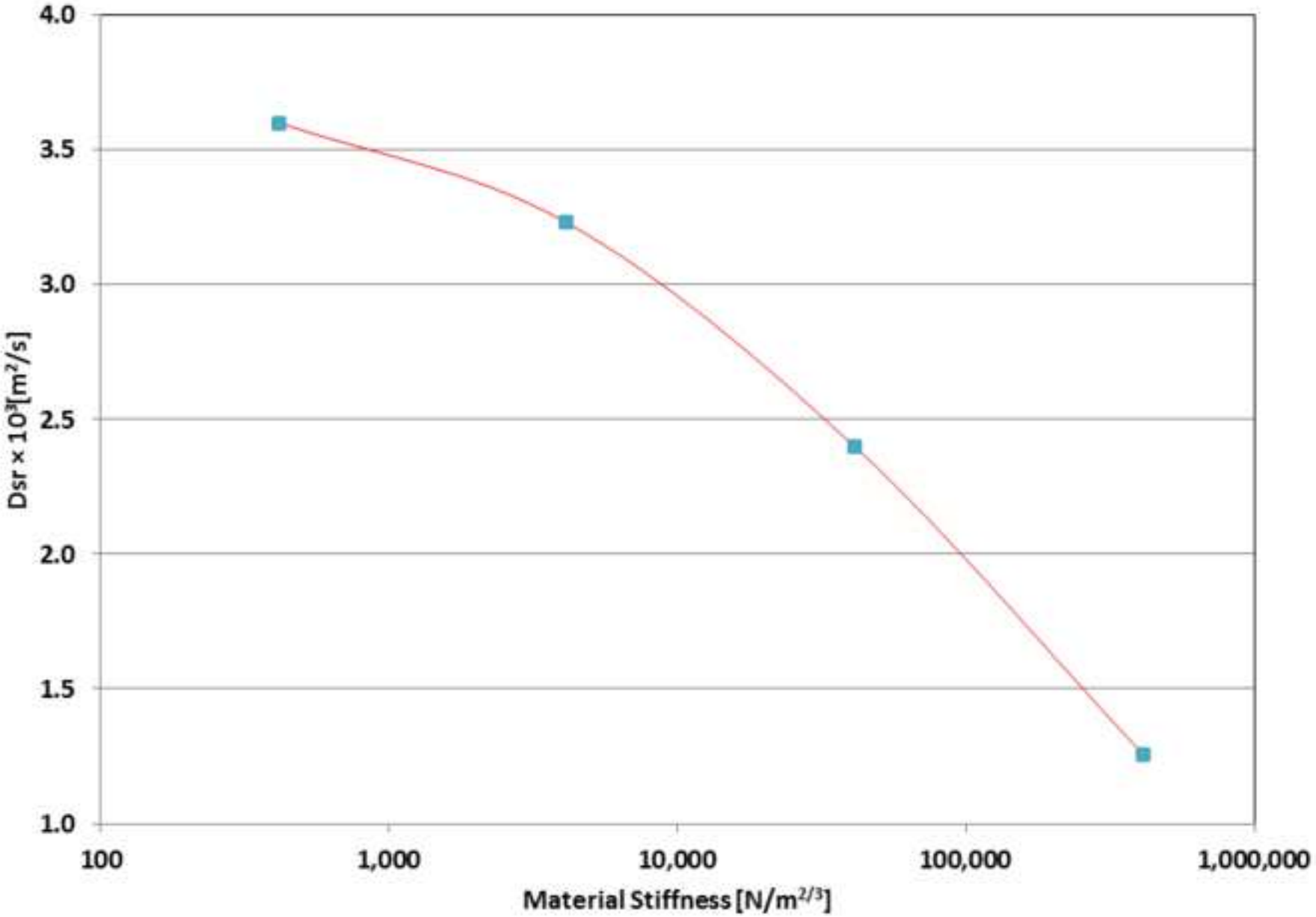
4.0
3.5
3.0
2.5
2.0
1.5
1.0
Dsr × 10³[m²/s]
100
1,000
10,000
100,000
1,000,000
Material Stiffness [N/m^2/3]

Figure 9

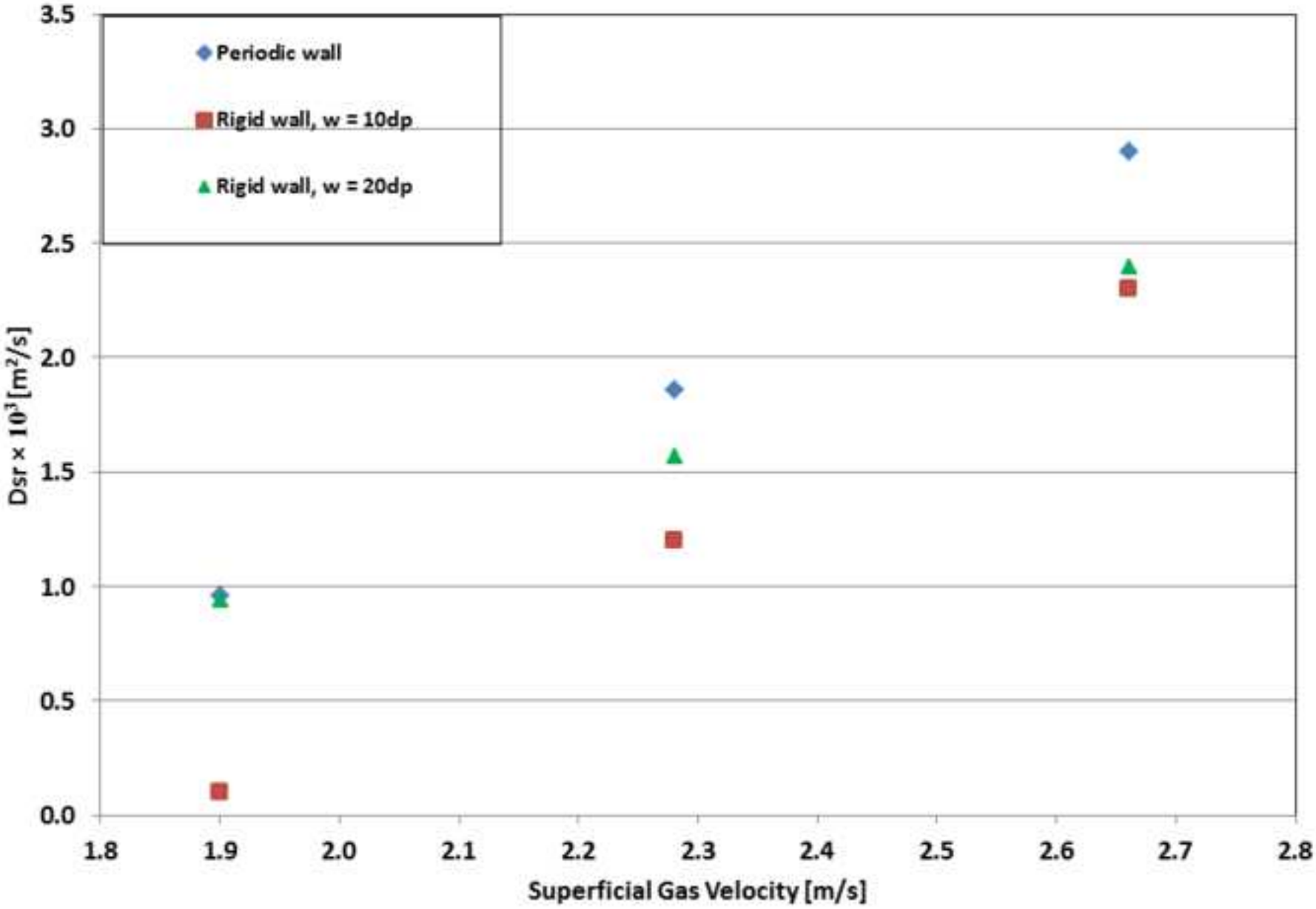
Periodic wall
Rigid wall, w = 10dp
Rigid wall, w = 20dp
Dsr × 10³ [m²/s]
3.5
3.0
2.5
2.0
1.5
1.0
0.5
0.0
1.8
1.9
2.0
2.1
2.2
2.3
2.4
2.5
2.6
2.7
2.8
Superficial Gas Velocity [m/s]

Figure 10

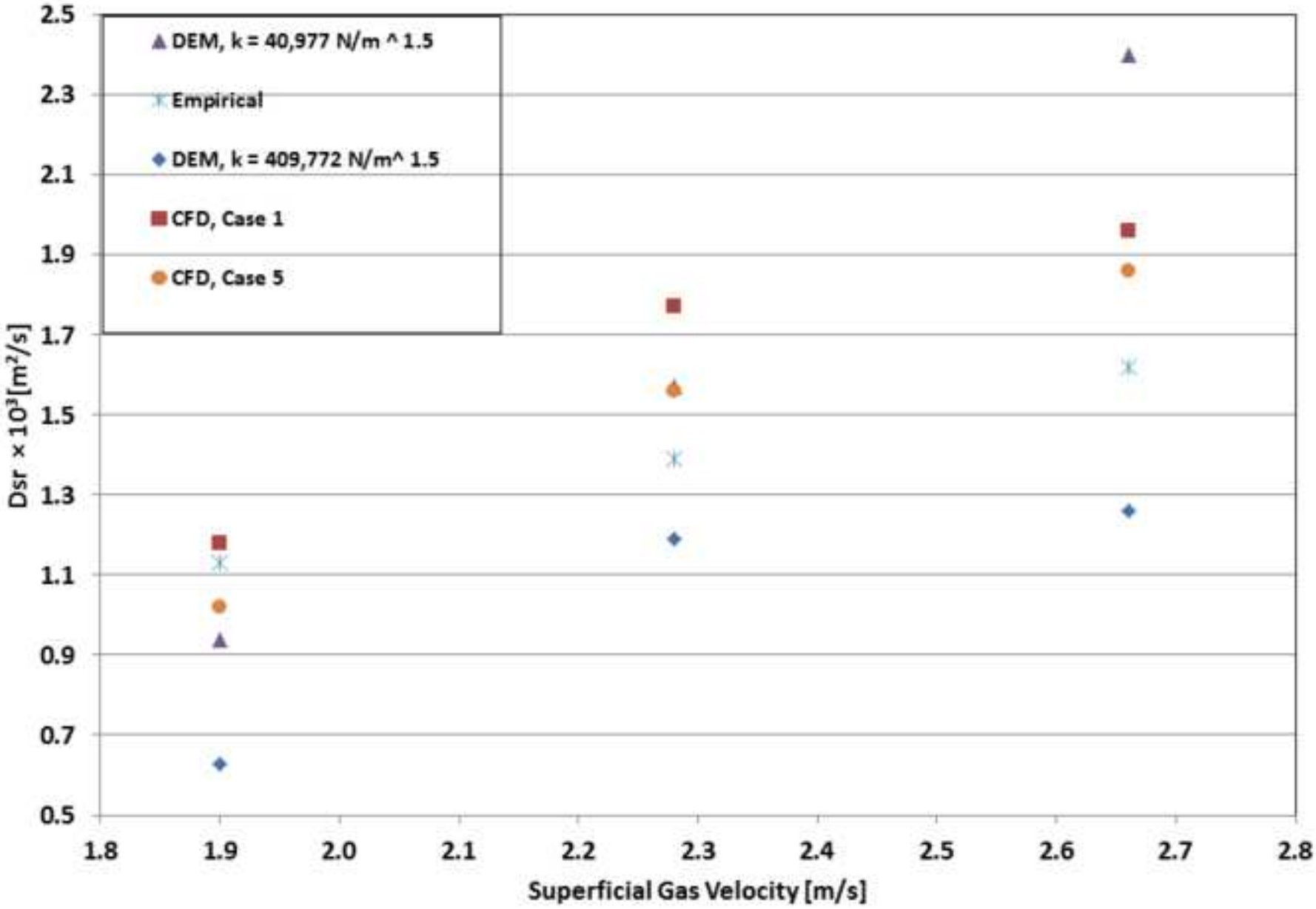
DEM, k = 40,977 N/m ^ 1.5
Empirical
DEM, k = 409,772 N/m^ 1.5
CFD, Case 1
CFD, Case 5
Dsr × 10³[m²/s]
2.5
2.3
2.1
1.9
1.7
1.5
1.3
1.1
0.9
0.7
0.5
1.8
1.9
2.0
2.1
2.2
2.3
2.4
2.5
2.6
2.7
2.8
Superficial Gas Velocity [m/s]

Table 1

Parameters	**Value**
Vessel height	0.35 m
Bed depth (thickness)	0.05 m
Bed Width	0.60 m
Superficial gas velocity	0.87 – 1.17 m/s
Particle diameter	491 μm
Particle density	2620 kg/m^3
Minimum fluidization velocity	0.20 m/s
Angle of internal friction	30^o
Restitution coefficient	0.90
Maximum particle packing	0.63
Bed height	0.05 m
Computational cell	0.005 m
Time-step	0.001 s

Table 1: CFD simulation parameters for Powder 1.

Table 2

	Frictional Pressure Model		Frictional Viscosity Model		Frictional Packing Limit	
Cases	**KTGF**	**J & J**	**Schaffer**	**J & J**	**0.50**	**0.61**
1	X		X			X
2	X		X		X	
3	X			X		X
4	X			X	X	
5		X		X	X	

Table 2: Summary of simulation cases.

Table 3

Conditions of particle	
Particle shape	Spherical
Diameter	3 mm
Density	1000 kg/m^3
Material stiffness	40,977 N/$m^{3/2}$
Restitution coefficient	0.90
Friction coefficient	0.2
Poisson ratio	0.33
Minimum fluidization velocity	0.76 m/s
Number	29,470
Conditions of gas	
Density	1.2 kg/ m^3
Viscosity	1.7×10^{-5} Ns / m^3
Simulation conditions	
Bed height	60 mm
Bed width	200 mm
Bed depth	60 mm (that is, 20 dp)
Superficial gas velocity	1.9 – 2.66 m/s
Particle time-step	10^{-6} s
Total simulated time	10 s

Table 3: DEM simulation parameters for Powder 2.

Table 4

Conditions of particle	
Diameter	3 mm
Density	1000 kg/m^3
Minimum fluidization velocity	0.76 m/s
Angle of internal friction	30^o
Restitution coefficient	0.90
Maximum particle packing	0.63
Conditions of gas	
Density	1.2 kg/ m^3
Viscosity	1.7×10^{-5} Ns / m^3
Simulation conditions	
Bed height	60 mm
Bed width	200 mm
Bed depth	60 mm
Superficial gas velocity	1.9 – 2.66 m/s

Table 4: CFD simulation parameters for Powder 2.

Figure Captions

Click here to download Supplementary MATLAB .fig files: Captions.docx